



**HAL**  
open science

## **DEM modelling for flow of cohesive lignocellulosic biomass powders: Model calibration using bulk tests**

John Pachón-Morales, Huy Do, Julien Colin, François Puel, Patrick Perre,  
Dingena Schott

### ► **To cite this version:**

John Pachón-Morales, Huy Do, Julien Colin, François Puel, Patrick Perre, et al.. DEM modelling for flow of cohesive lignocellulosic biomass powders: Model calibration using bulk tests. *Advanced Powder Technology*, 2019, 30 (4), pp.732-750. 10.1016/j.appt.2019.01.003 . hal-02294258

**HAL Id: hal-02294258**

**<https://hal.science/hal-02294258v1>**

Submitted on 11 Sep 2020

**HAL** is a multi-disciplinary open access archive for the deposit and dissemination of scientific research documents, whether they are published or not. The documents may come from teaching and research institutions in France or abroad, or from public or private research centers.

L'archive ouverte pluridisciplinaire **HAL**, est destinée au dépôt et à la diffusion de documents scientifiques de niveau recherche, publiés ou non, émanant des établissements d'enseignement et de recherche français ou étrangers, des laboratoires publics ou privés.

***To cite this article:*** J. PACHÓN-MORALES, H. DO, J. COLIN; F. PUEL, P. PERRE and D. SCHOTT, (2019) DEM modelling for flow of cohesive lignocellulosic biomass powders : model calibration using bulk tests, *Advanced Powder Technology* 30, 732–750 <https://doi.org/10.1016/j.apt.2019.01.003>

## **DEM modelling for flow of cohesive lignocellulosic biomass powders: Model calibration using bulk tests**

John Pachón-Morales<sup>a\*</sup>, Huy Do<sup>b</sup>, Julien Colin<sup>a,c</sup>, François Puel<sup>a</sup>, Patrick Perré<sup>a,c</sup>, Dingena Schott<sup>b</sup>

<sup>a</sup>LGPM, CentraleSupélec, Université Paris-Saclay, 3 rue Joliot-Curie, 91192 Gif-sur-Yvette, France

<sup>b</sup>Section Transport Engineering and Logistics, Department Maritime & Transport Technology, Faculty of Mechanical, Maritime and Materials Engineering, Delft University of Technology, Mekelweg 2, 2628CD Delft, The Netherlands

<sup>c</sup>LGPM, CentraleSupélec, Université Paris-Saclay, SFR Condorcet FR CNRS 3417, Centre Européen de Biotechnologie et de Bioéconomie (CEBB), 3 rue des Rouges Terres, 51110 Pomacle, France

---

\* Corresponding author

E-mail addresses : (J. Pachón-Morales) [john.pachon@centralesupelec.fr](mailto:john.pachon@centralesupelec.fr),  
(J. Colin) [julien.colin@centralesupelec.fr](mailto:julien.colin@centralesupelec.fr)

## Abstract

Biomass feeding problems greatly hinder the industrialization of entrained-flow gasification systems for production of 2<sup>nd</sup> generation biofuels. Appropriate DEM modelling could allow engineers to design solutions that overcome these flow problems. This work shows the application of a DEM calibration framework to produce a realistic, calibrated and efficient material model for lignocellulosic biomass. A coarse (500-710  $\mu\text{m}$ ) and a fine (200-315  $\mu\text{m}$ ) sieving cuts of milled poplar were used in this study. The elongated shape and the cohesive behavior were respectively simulated using a coarse-grained multisphere approach and a cohesive SJKR contact model. Measurements of three physical responses (angle-of-repose, bulk density, a retainment ratio) allowed calibration of the sliding ( $\mu_s$ ) and rolling friction ( $\mu_r$ ) coefficients and the cohesion energy density ( $CED$ ). Using a statistical analysis, the most influential calibration parameters for each bulk response were identified. A Non-Dominated Sorting Genetic Algorithm was used to solve the calibration multi-objective optimization problem. Several sets of optimal solutions reproduced accurately the three physical responses and the experimental shear responses were closely reproduced by simulations for the population of coarse particles. The DEM calibration framework studied here aims to produce material models useful for assessing flow behavior and equipment interaction for biomass particles.

**Keywords:** Woody biomass powder, Discrete Element Method, Parameter calibration, Multi-objective optimization, Cohesion

## Highlights

- A realistic and calibrated DEM model for cohesive biomass powder is obtained.
- A multisphere representation reproduces the elongated shape of particles.
- A coarse-graining approach is used to reduce simulations runtime.
- Three contact parameters are calibrated using a genetic algorithm of optimization.
- Optimal solutions reproduce accurately the experimental physical responses.

## 1. INTRODUCTION

Entrained-flow biomass gasification appears one of the most suitable technology for production of second-generation biodiesel, mainly because of its great flexibility for treating a variety of biomass feedstock and because it generates the purest syngas [1,2]. This process requires lignocellulosic biomass to be fed in sub-millimetric powder form. However, a major technical obstacle for a cost-effective industrialization of this technology is related to the feeding, handling and transport of biomass particles. Unsteady flow and equipment blockages are linked to the fibrous and cohesive characteristics of biomass powders, as well as to their relatively low weight per unit volume. Despite the importance of achieving trouble-free flow and the frequency of feeding problems, much more attention has been devoted typically to reactor design and operation than to biomass feeding and flow characterization [3].

Evaluation and design of biomass feeding systems need a full comprehension of the effects of biomass intrinsic properties such as particle size and shape on the flow characteristics. For this purpose, the use of numerical simulations constitutes a powerful alternative to experimental approaches, which are often limited regarding the exploration domain of influential variables, the presence of intrinsic sample variability, or as for the experimental difficulty of isolating individual parameter effects.

The discrete element method (DEM) is the most frequently implemented method when designing and modelling particulate bulk solid handling systems. The particulate system is modelled as an assembly of singular discrete and interacting particles. Particle positions, velocity and forces acting on each particle are calculated at small intervals based on a force-displacement contact law and Newton's second law of motion [4]. Whilst DEM simulations are being used more and more extensively in a wide range of applications, the question of whether DEM is capable of producing quantitative predictions, rather than only qualitative representations of a granular solid remains largely unanswered. Therefore, one of the main constraints for application of DEM in an industrial context is the determination of the input parameters needed to adequately simulate the behavior of particulate systems.

Due to the disparity between physical properties obtained via traditional tests and the simulation parameters such as stiffness, sliding and rolling friction, calibrations tests are essential. Though scarce, research in the area of calibrating and modelling biomass particles includes the determination of physical

properties of briquettes to be used in DEM models by Ramirez-Gomez et al. [5] and the study through DEM of feeding systems for wood-chips by Rackl et al. [6]. More research remains to be done regarding measurements or calibrations of biomass particles at a sub-millimetric and powder scale.

Calibration of biomass feedstocks can be complicated by the elastic, fibrous or stringy bulk behavior related to individual particle characteristics and requires adaptation of existing contact models [7]. Integration of realistic shape models remains also of major concern. Indeed, previous DEM investigations have primarily focused on spherical particles. However, non-spherical powders such as biomass powders are more often encountered in industrial applications. Recent advances in computing speed and power have opened the way to more complex approaches for non-spherical particles representation. Possible shape descriptors in two and three dimensions are multi-sphere approaches, ellipses or ellipsoids, super-quadric bodies, discrete functions, shape combinations, composite particles and flexible fibers models. An overview of possible methods for DEM particles representation is given in [8–11].

Another major challenge for DEM simulations is the limitation regarding the number of particles that can be modelled in a reasonable time period. Most of DEM simulations considers a restricted number of particles (in the order of hundreds of thousands) with diameters in the order of some millimeters to achieve a reasonable computing time [12]. In industrial practice, however, it is often necessary to deal with billions of particles within a wide range of particle sizes. For this reason, it is unavoidable to upscale the particle size to reduce the total number of particles and thus the computational time. Several approaches of particles scale-up have been developed and can be generally sorted as: “exact scaling” [13–15], “coarse-graining” [16–19] and “cutting-off” [19,20]. Exact scaling has no advantage regarding the reduction of the number of particles, so the computation time can be reduced, as scaling factors are applied to both the equipment geometries and the particles size. Coarse-graining is defined as the reduction of computational cost by replacing actual particles by scaled representative models [17]. The scaling factor in the coarse-graining approach is only applied to the radius or volume of the particle, while the geometries of the equipment are not scaled. Coarse-graining approaches has been widely applied to spherical cohesionless materials [16,17,21,22] but, besides works by Thakur et al. [23], little research about its relevance on simulation of elongated and cohesive particles has been made.

The main aim of this paper is to describe the application of a calibration framework proven successful for spherical materials [24–26] to biomass powders which are constituted of sub-millimetric elongated particles and have cohesive characteristics. In addition, other subjacent goals are: (i) to explore the usefulness of a coarse-graining approach for simulation of a large number of elongated biomass particles (ii) to assess the influence of DEM calibration parameters on the bulk properties of the material (iii) to illustrate the trade-offs encountered when dealing with multiobjective calibration and the multiplicity of valid solutions. In a broader perspective, this work intends to establish calibrated, realistic and efficient material models allowing the assessment of the effects of biomass particle properties on bulk behavior. This will allow the study of efficient design strategies of handling equipment for powdered lignocellulosic biomass.

## 2. MATERIALS AND METHODS

### 2.1. Samples preparation and particle size and shape characterization

Poplar was chosen as a representative for lignocellulosic biomass as it is a promising energy crop, namely due to its fast growth in temperate climates. Additionally, the development of poplar genotypes with improved yield, higher pest resistance, increased site adaptability and easy vegetative propagation has made poplar a commercially valuable energy crop [27,28]. The poplar tree selected for the present study came from a forest located in *La Suippe* valley in Auménancourt-le-Petit (France). The tree was shopped and cut in boards that were subsequently dried.

Samples of 60x80x15 mm<sup>3</sup> were cut from the boards and ground using a Retsch SM300 cutting mill with a bottom sieve of 1 mm trapezoid holes at the outlet. The powders obtained after grinding were sieved to obtain two well differentiated sieving cuts representative of coarse and fine particles. A vibratory sieve shaker Retsch AS 200 at a frequency of 60 Hz for 20 minutes was used along with sieves of opening 500 µm and 710 µm for the coarse cut and 200 µm and 315 µm for the fine cut.

A *Sympatec-QICPIC* morphological particle size analyzer was used to obtain biomass particles size distribution (PSD) after sieving [29]. The values of the descriptors of particles size distribution and shape distribution are listed in Table 1. The minimum value of the Feret diameters over all orientations of the particle is used as the magnitude characterizing particles size. The 50th centile of the cumulative volume

distributions ( $x_{50}$ ) was taken as a mean size descriptor of each size distribution. PSD span ( $S_x$ ) was calculated from values of the 90th and 10th centiles as:

$$S_x = (x_{90} - x_{10}) / (x_{90} + x_{10}) \quad (1)$$

Particle shape was characterized through the aspect ratio,  $a$ , which is defined as the ratio between the minimum and the maximum Feret diameters for a given particle. Mean values of the aspect ratio,  $a_{50}$  were calculated as the 50th centile of the cumulative aspect ratio distributions, and the aspect ratio span  $S_a$  is defined by:

$$S_a = (a_{90} - a_{10}) / (a_{90} + a_{10}) \quad (2)$$

where  $a_{90}$  and  $a_{10}$  correspond to the 90th and 10th centiles of the aspect ratio distribution, respectively.

Table 1. Samples nomenclature and size/shape characteristics.

Sample	Sieving cut ( $\mu\text{m}$ )	$x_{50}$ ( $\mu\text{m}$ )	$x_{90}$ ( $\mu\text{m}$ )	$x_{10}$ ( $\mu\text{m}$ )	$S_x$	$a_{50}$	$S_a$
1 (Coarse sieving cut)	500-710	746	1092	519	0.36	0.38	0.49
2 (Fine sieving cut)	200-315	352	513	243	0.36	0.42	0.53

## 2.2. Bulk behavior tests

The first stage in the DEM calibration procedure consists of choosing an adequate number of bulk experiments that characterize particles bulk behavior. Suitable calibration measurements should: (i) be easy to implement in laboratory tests and time-efficient, (ii) produce sufficiently discriminating values from variations in material properties and (iii) be highly reproducible and repeatable. From this point of view, the bulk setups described hereafter have been proven suitable for cohesive materials such as biomass powders, according to preliminary tests made as part of this work.

### 2.2.1. Angle-of-Repouse from bulk solid heaps

Angle-of-repose measurements have been extensively used in previous research for calibration of DEM models for bulk materials [22,30–32], with special focus on non-cohesive materials.

Conventional methods for measuring the AoR such as the lifting cylinder test [19] were tested in the preliminary stages of this work. Due to the cohesive strength and interlocking effects within biomass

samples, stable structures were formed regardless of the filling method or the cylinder size. As a result, this method was unsuccessful to obtain a heap from which the AoR could be calculated.

A poured AoR method adapted from [33,34] was used in this work. Repeatable measurements of the AoR were attained by pouring 40 g of the powders manually over a stainless steel inclined surface, and then measuring the slope of the heap formed over a flat paper surface by the particles flowing out of the ramp (Figure 1). The inclination of the surface was fixed to be  $\theta = 40^\circ$  for the coarse samples and  $\theta = 50^\circ$  for the finer. The inclination was measured using a calibrated angle-meter fixed to the inclined surface. Flow rate was controlled manually to avoid accumulation of the particles on the surface and set to be around 0.5 g/s. A camera taking images from a side view of the heap was placed always at the same position during the experiments. Each measurement was repeated seven times.

Image analysis using ImageJ [35] allowed heap's profile extraction and AoR determination by linear regression. Shape and symmetry of the heap were occasionally influenced by flow intermittencies, so values of AoR were calculated from the left side of the heap as it was the region less sensitive to abrupt perturbations.

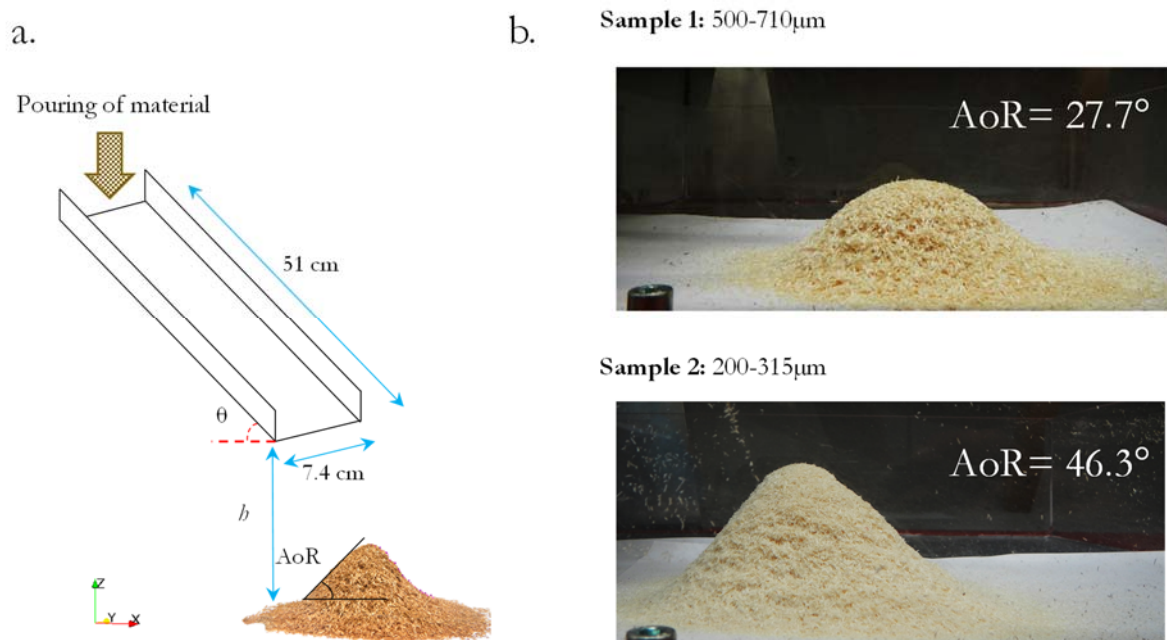


Figure 1. AoR setup: a. Heap formation and main setup dimensions; b. Examples of biomass powders heaps.

For calculation of the AoR, a direct linear regression procedure using the heap's surface line instead of an indirect measurement from the heap's diameter and height [36] was preferred. Indeed, several authors



have shown that there could be significant differences in AoR measurements depending on the chosen method of calculation, especially for asymmetric heaps [37–39]. Indirect methods can be very sensitive to the choice of the extreme points of the heap, while a calculation including the entire profile line represents better the pile shape. In all cases, relatively symmetric heaps were obtained and determination coefficients ( $r^2$ ) of linear regressions were always over 0.95.

### *2.2.2. Bulk density*

Loose bulk density,  $\rho_b$  in  $\text{kg}/\text{m}^3$ , refers to the ratio of the mass of bulk sample  $m_i$  over its aerated volume  $V_i$  ( $\rho_b = m_i / V_i$ ). It represents the most loosely packed density of the material. Around 50 ml of oven-dried samples were smoothly poured into a graduated plastic vessel, and the mass of solid was then recorded. Each measurement was repeated for six refills using different oven-dried powder of the same sample.

### *2.2.3. Rectangular container test*

Preliminary studies showed that calibrated parameters for biomass powders using only information from AoR and bulk density measurements did not represent a realistic cohesive flow behavior when particles settled inside a container. Rectangular containers, also called “shear box” or “ledge test”, have been used in previous research for DEM calibration tests [19,32,40]. Therefore, a rectangular container with adjustable walls was used in this work for complementary calibration (Figure 2). Walls were adjusted to adapt to the available volume of sample, so that the final dimensions of the container were 25 cm (height) x 6 cm (length) x 5.7 cm (width). The bulk material was poured in the volume and the powder’s surface was carefully kept flat at the end of the pouring. The final height of the stack was 7 cm. The cabin lid of the container was then lifted, and particles were allowed to flow out of the volume.

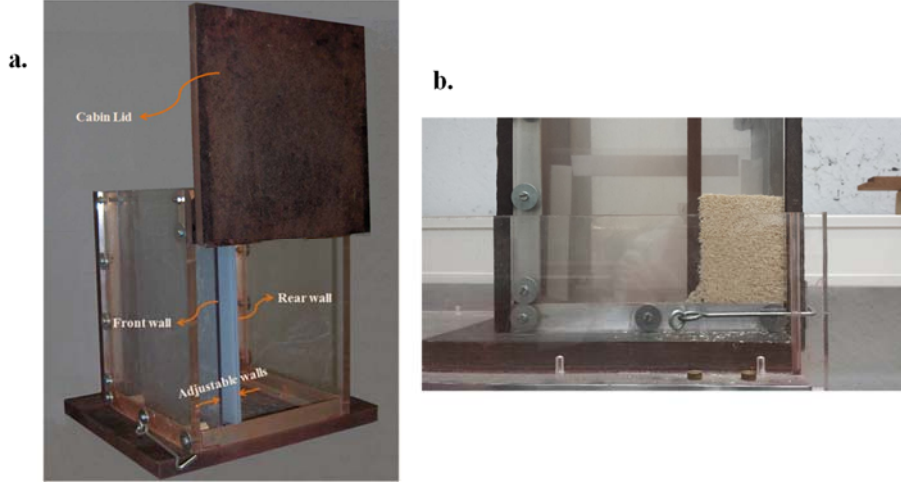


Figure 2. Rectangular container device. a. Container. b. Example of a sample inside a volume reduced by the adjustable walls.

For simulation purposes, the retainment ratio  $P$  is defined by:

$$p = \frac{m_r}{m_0} \quad (3)$$

where  $m_r$  is the mass remaining in the volume after the cabin lid is lifted, and  $m_0$  corresponds to the mass initially poured inside the container.

#### 2.2.4. Ring shear tester

A RST-XS Schulze ring shear tester [41,42] was used to assess the flow properties of the biomass powders. The ring shear tester is a widely-used device to measure flow properties of powders, including unconfined yield strength, angle of internal friction and wall friction. The standard procedure leads to results with low variability [41]. A consolidation stress  $\sigma_{pre} = 5$  kPa, considered as representative of the stress range for industrial applications, was tested [43]. Three shear points at 25%, 50% and 75 % of  $\sigma_{pre}$  were used to determine the yield locus of each sample. The yield locus curves were regressed from experimental points by a linear regression.

### 2.3. DEM simulations setup

This section contains an overview of the DEM contact model used in this work as well as the procedure for representing particles characteristics through a multisphere and coarse-graining approach. Then the simulation setup for each bulk test is presented.

### 2.3.1. DEM contact model

In this study, simulations were run using the public version of LIGGGHTS 3.8.0 DEM code [44], on a E5-2620 v4 2.10 GHz Intel® Xeon® machine with 125.8 GB of RAM, and with parallelization on 8 cores. A Hertz-Mindlin contact model along with an elastic-plastic spring-dashpot (EPSD2) rolling friction model and a simplified Johnson-Kendall-Roberts (SJKR) cohesion model were used. The Hertz-Mindlin model stands as the most commonly used contact model due to its efficient and accurate force calculations. A representation of the contact model, accounting for a spring elastic force, a viscous damping and a frictional slider in the tangential direction, is shown in Figure 3 [45]. At any time  $t$ , the equations governing the translational and rotational motion of particle  $i$  of mass  $m_i$  and radius  $R_i$  can be written as:

$$m_i \frac{d\mathbf{v}_i}{dt} = \sum_j (\mathbf{F}_{ij}^e + \mathbf{F}_{ij}^d + \mathbf{F}_{ij}^{coh}) + m_i \mathbf{g} \quad (4)$$

and

$$I_i \frac{d\boldsymbol{\omega}_i}{dt} = \sum_j (\mathbf{T}_{ij}^t + \mathbf{T}_{ij}^r) \quad (5)$$

Where  $\mathbf{v}_i$  and  $\boldsymbol{\omega}_i$  are the translational and rotational velocities of particle  $i$ , and  $I_i$  is the moment of inertia of the particle. The forces involved are: the gravitational force  $m_i \mathbf{g}$  and the forces between particles (and between particles and walls) which include the an elastic force  $\mathbf{F}_{ij}^e$ , a viscous damping component  $\mathbf{F}_{ij}^d$  and cohesive contributions through the  $\mathbf{F}_{ij}^{coh}$  term. The torque acting on particle  $i$  due to particle  $j$  includes two components:  $\mathbf{T}_{ij}^t$  which is generated by the tangential force and causes particle  $i$  to rotate, and  $\mathbf{T}_{ij}^r$ , the rolling friction torque generated by asymmetric distribution of normal contact force and slows down the relative rotation between particles in contact [46]. If particle  $i$  undergoes multiple interactions, the individual interaction forces and torques sum up for all particles interacting with particle  $i$ . The equations for calculation of the particle-particle interaction forces within the Hertz-Mindlin contact model are listed in

Table 2.

Table 2. Equations for calculations of forces and torques on particle  $i$  according to the Hertz-Mindlin model.

Force or torque contribution	Equation
Normal elastic force, $\mathbf{F}_{ij,n}^e$	$k_n \delta_{ij,n} = -\frac{4}{3} Y_{eff} \sqrt{R_{eff}} \delta_{ij,n}^{3/2}$
Normal damping force, $\mathbf{F}_{ij,n}^d$	$\gamma_n \mathbf{v}_{ij,n} = -\frac{2\sqrt{5/6} \ln(e)}{\sqrt{\ln^2(e) + \pi^2}} \sqrt{2Y_{eff} (R_{eff} \delta_{ij,n})^{1/2}} m_{eff} \mathbf{v}_{ij,n}$
Tangential elastic force, $\mathbf{F}_{ij,t}^e$	$k_t \delta_{ij,t} = -8G_{eff} \sqrt{R_{eff}} \delta_{ij,n} \delta_{ij,t}$
Tangential damping force, $\mathbf{F}_{ij,t}^d$	$\gamma_t \mathbf{v}_{ij,t} = -\frac{2\sqrt{5/6} \ln(e)}{\sqrt{\ln^2(e) + \pi^2}} \sqrt{8G_{eff} (R_{eff} \delta_{ij,n})^{1/2}} m_{eff} \mathbf{v}_{ij,t}$
Coulomb friction limit	$\delta_{ij,t}$ truncated to satisfy $\mathbf{F}_{ij,t}^e \leq \mu_s \left  \mathbf{F}_{ij,n}^e + \mathbf{F}_{ij,n}^d + \mathbf{F}_{ij,n}^{coh} \right $
Torque by tangential forces, $\mathbf{T}_{ij}^t$	$\mathbf{R}_{ij} \times (\mathbf{F}_{ij,t}^e + \mathbf{F}_{ij,t}^d)$
Torque by rolling friction, $\mathbf{T}_{ij}^r$	EPSD2 model

Where  $1/m_{eff} = 1/m_i + 1/m_j$ ,  $1/R_{eff} = 1/R_i + 1/R_j$ ,  $1/\nu_{eff} = (1-\nu_i^2)/\nu_i + (1-\nu_j^2)/\nu_j$ ,  $1/G_{eff} = 2(2-\nu_i)(1+\nu_i)/\nu_i + 2(2-\nu_j)(1+\nu_j)/\nu_j$ ,  $\mathbf{R}_{ij} = R_i(\mathbf{r}_j - \mathbf{r}_i)/(R_i + R_j)$ ,

$e$  : coefficient of restitution,  $Y$  : Young's modulus,  $G$  : shear modulus,  $\nu$  : Poisson's ratio.

Regarding rolling friction modelling, the alternative elastic-plastic spring-dashpot model EPSD2 [47] adds an additional torque contribution to the particles motion given by:

$$\mathbf{T}_{ij}^r = \mathbf{T}_{ij}^{r,k} = -k_r \Delta \boldsymbol{\theta}_{r,ij} \quad (6)$$

Where  $\mathbf{T}_{ij}^{r,k}$  is a torque component modelled as a mechanical spring,  $k_r$  is the rolling stiffness and  $\Delta \boldsymbol{\theta}_{r,ij}$  is the incremental relative rotation between two particles. The torque contribution is truncated so:

$$\mathbf{T}_{ij}^{r,k} \leq \mathbf{T}_{ij}^{r,max} = \mu_r R_{eff} \mathbf{F}_n \quad (7)$$

Where  $\mu_r$  is the rolling friction coefficient,  $R_{eff}$  the effective radius and  $\mathbf{T}_{ij}^{r,max}$  being the limiting spring torque which is achieved at a full mobilization rolling angle  $\theta_r^m$ . In the EPSD2 model, the rolling stiffness  $k_r$  is defined as:

$$k_r = k_t R_{eff}^2 \quad (8)$$

Where  $k_t$  corresponds to the tangential (i.e. shear) stiffness. Figure 3b shows the mechanism of rolling resistance and the physical meaning of the coefficient of rolling friction  $\mu_r$ , which is a scalar value that represents the eccentricity of the resulting normal force exerted by a surface on a rolling particle. In the EPSD2 model  $\mu_r$  does not appear explicitly in the expression for the rolling stiffness (as for CDT or EPSD models) but instead is used for restricting the maximum spring torque.

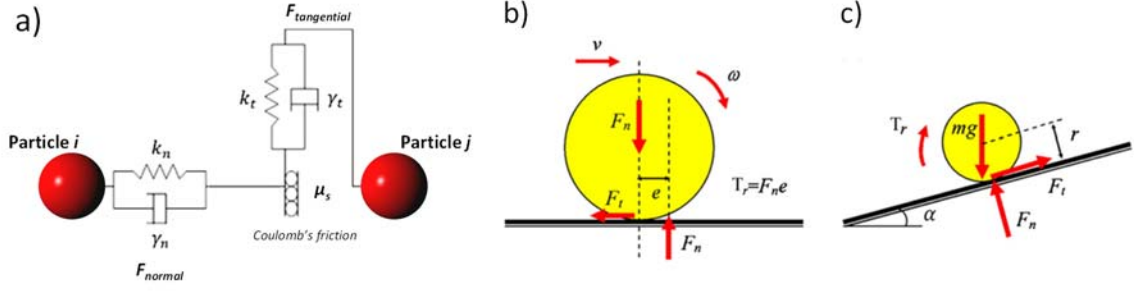


Figure 3. Schematic representation of the contact model used in this study: a) Hertz-Mindlin contact model; b) Mechanism of rolling resistance; c) rolling resistance angle [48]

The simplified Johnson-Kendall-Roberts model (SJKR) [49], used to simulate cohesion between particles, adds an additional normal force  $\mathbf{F}_{ij,n}^{coh}$  tending to maintain the contact between two particles, given by:

$$\mathbf{F}_{ij,n}^{coh} = CED \cdot A \quad (9)$$

Where  $CED$  is the Cohesive Energy Density in  $J/m^3$  and  $A$  is the particle contact area.

### 2.3.2. Particles representation

The biomass powders were modelled as monodispersed populations of clumps of spheres (multi-sphere method). Spheres comprising a multi-sphere particle are fixed in position relative to each other and may overlap to approximate more closely to the actual particle shape [50]. The multi-sphere method stands as one of the most general and most efficient method for representing shape within DEM. By using a multi-sphere approach it is possible to ensure computational efficiency for contact detection and force calculation and it is widely implemented in many DEM codes [51,52]. Multi-sphere representations have previously been used for describing flow in silos of agricultural resources such as maize and rice grains [53,54]. When using a multisphere approach, finding a trade-off between particles representation accuracy and DEM run time is essential. For instance, in their study with maize grains, Markauskas et al. [53] found that models with 6 sub-spheres successfully reproduced discharging time in silos, but similar results could be obtained with 4 sub-spheres using another set of calibration parameters.

In order to reduce the number of spheres needed to represent one single particle, in this study individual spheres were oriented over one single longitudinal axis, so the particles were needle-shaped (Figure 4). To approximate the true morphology obtained by PSD measurements, a simplified model for particle

representation was proposed. In this model, the number of spheres in a clump,  $n_{sph}$ , is function of the particles mean size ( $x_{50}$ ), the mean aspect ratio ( $a_{50}$ ) and an overlapping factor  $c$ .

The overlapping factor can be expressed as  $c = \lambda / x_{50}$ , where  $\lambda$  is the overlapping distance between adjacent spheres in  $\mu\text{m}$  (Figure 4a). A value of  $c = 0$  means two spheres touching each other at one single point and  $c = 1$  represents a total overlap between two contiguous spheres. As  $c$  increases the effective roughness of the particle decreases. Previous work [52] suggested that reducing surface roughness by increasing the number of spheres per clump did not necessarily lead to a better approximation of particles behavior. A value of  $c$  of 20% was chosen as it is considered a good trade-off between the accuracy of particles representation and the number of spheres needed.

The diameter of each sphere is set to be equal to the mean minimum Feret diameter of the population,  $x_{50}$ . Therefore, the length of the clump ( $l_{clump}$ ), which corresponds to the mean maximum Feret diameter, can be calculated as follows:

$$l_{clump} = x_{50} / a_{50} = n_{sph} \cdot (x_{50} - \lambda) + \lambda \quad (10)$$

So, from the definitions of  $a_{50}$  and  $c$ , the number of spheres needed per clump is:

$$n_{sph} = \frac{1/a_{50} - c}{1 - c} \quad (11)$$

The calculated values were rounded to the closest integer and the length of the clump recalculated accordingly.

Calculation of bulk density from simulations needs the value of the mass of each clump, which is computed from the clump's volume, given by:

$$V_{clump} = n_{sph} \pi r^3 \left( \frac{4}{3} - \frac{n_{sph} - 1}{12n_{sph}} (6 - 2c)(4c^2) \right) \quad (12)$$

Where  $r$  is the spheres radius  $r = x_{50} / 2$ . *Table 3* shows the model parameters used for particles representation. For the sake of comparison with spherical models for particle representation, the equivalent radius of a sphere having the same volume as one individual clump ( $R_{eq}$ ) is also reported.

Table 3. Parameters of multispheres model for particles representation

	Sample 1	Sample 2
$n_{sph}$	3	3
$r$ ( $\mu\text{m}$ )	373	176
$l_{clump}$ ( $\mu\text{m}$ )	1940	915
$V_{clump}$ ( $\text{mm}^3$ )	0.6282	0.0658
$R_{eq}$ ( $\mu\text{m}$ )	531	251

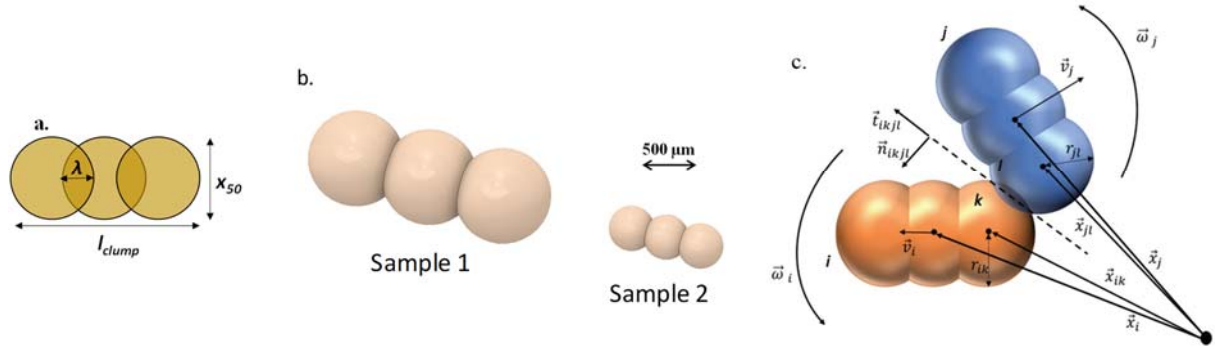


Figure 4. Particles representation for biomass samples. a. Nomenclature of main dimensions in a clump. b. Samples multispheres models (true relative size). c. Representation of a collision between spheres  $k$  and  $i$  within two multi-sphere particles ( $\vec{t}_{ikjl}$ : tangential unit vector,  $\vec{n}_{ikjl}$ : normal unit vector of contact zone) [55].

### 2.3.2.1. Scaling up particle size

Since parameters calibration commonly involves running an extensive amount of simulations, the representation of the actual number of particles used during the bulk tests would not be possible within a realistic frame time. A scaling factor,  $SF$ , can be defined as the ratio between the simulated particle radius and the actual value from PSD. As shown in Figure 5a, the computational time required to simulate one real-time second of heap formation for sample 1 significantly decreases by increasing the scaling factor, as the number of particles ( $n_{particles}$ ) decreases. A series of test runs were performed to assess the effect of scaling particle size up on the AoR of the heap formed using non-calibrated parameters ( $\mu_s = 0.9$ ,  $\mu_r = 0.5$  and  $CED = 0 \text{ J/m}^3$ ). Testing values of  $SF$  over 7 leads to high uncertainty on the value of AoR as the number of particles is not enough to form a proper heap. The linear downward trend showed in Figure 5b clearly indicates that scaling effects on the AoR are not negligible. This is in contrast with results by Roessler and Katterfeld [19] who found AoR to be scale-independent. However, their conclusions referred to the case of

quasi-static formation of a heap using lifting cylinder setups, which is hardly the flow condition of particles forming the heap in this work.

In the aim of reducing computing time, a coarse-graining approach was followed and a trade-off between the actual representation accuracy and the calculation effort was made by scaling particles size up by a factor of 4. Since the effect of the scaling factor on the bulk responses could vary depending on the values of the calibrated parameters, calibration was made using the actual values from experiments (instead of, for example a value corrected by the  $SF$  using the trend of Figure 5b). This allowed to run a typical heap formation simulation in approximately 1 hour for coarse particles and in 8 hours for fine particles, while several weeks would be needed to run a single simulation of fine particles at their actual size.

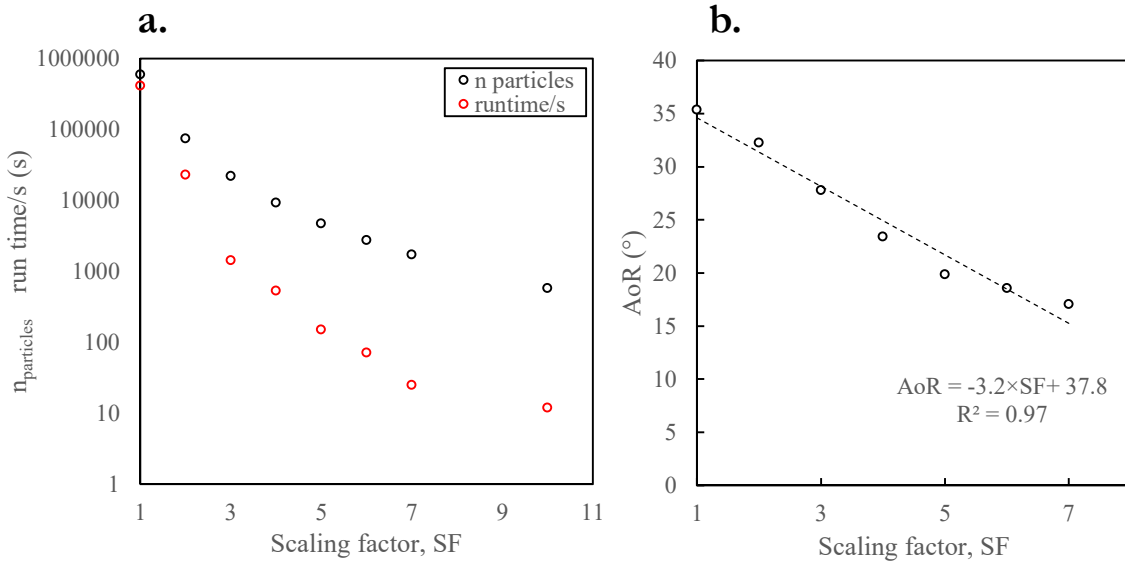


Figure 5. Influence of scaling particles size up for sample 1: a. Number of particles and simulation time. b. Angle-of-repose value.

### 2.3.3. Time-step

Because of the explicit numerical scheme used for DEM integration, only relatively small time-step values ( $\Delta t$ ) guarantee stable simulations. A common strategy to fix a value for  $\Delta t$  is based on the Rayleigh ( $\Delta T_R$ ) and Hertz ( $\Delta T_H$ ) critical time-steps, calculated as [56]:

$$\Delta T_R = \frac{\pi r \sqrt{\rho / G}}{0.1631\nu + 0.8766} \quad (13)$$



$$\Delta T_H = 2.87 \left( \frac{m_{eff}^2}{r_{eff} Y_{eff}^2 V_{max}} \right)^{0.2} \quad (14)$$

Where  $r$  is the minimum particle radius in the system and  $V_{max}$  is the maximum relative velocity. The other parameters correspond to those defined previously in Section 2.3. In this work, both critical time-steps were calculated during DEM integration and the simulation time-steps were fixed to be lower than 10% of  $\Delta T_R$  and  $\Delta T_H$ . Values for both samples are reported in *Table 4*.

#### 2.3.4. *Angle-of-Repose and bulk density determination from simulations*

The experimental test shown in Figure 1 was numerically replicated using LIGGGHTS. To reduce the simulation time, the simulated conveyor length is reduced to a half of the experimental length. The angle-of-repose and bulk density were calculated using the positions of the particles in the heap at the end of the simulation when all the particles are in a stable state. To avoid underestimation of those two bulk values, the particles non-connected to the heap were not considered in the calculation.

As for the experiments, the angle of repose in the  $xz$ -plane was calculated for the left side of the heap. At first, the positions of the particle at the top and the particle at the leftmost of the heap were identified to determine the domain of the angle-of-repose slope. The particles in this domain were then binned into 20 equally-spaced horizontal layers. For each layer, the  $x$  and  $z$  coordinates of the top particle on the slope were identified. The angle of repose was then determined using linear regression of these 20  $x$ - $z$  coordinates on the slope. The number of layers = 20 was chosen as it is high enough to produce stable values of AoR and high correlation coefficient values for all calculations.

The bulk density of the heap was calculated from its bulk mass divided by its aerated volume. The bulk mass is equal to the mass of one clump multiplied by the number of clumps in the heap. The concept of numerical integration in volume calculation was implemented in a C++ algorithm to estimate the aerated volume of the heap (analytically as the left-hand side of Eq. 15, and numerically “discretized”, as the right-hand side of the Eq. 15):

$$\iint_{x_{min}, y_{min}}^{x_{max}, y_{max}} h(x, y) dx dy \approx \sum_1^{n_x} \sum_1^{n_y} h(x_i, y_i) \Delta x \Delta y \quad (15)$$

where  $x_{min}, x_{max}, y_{min}, y_{max}$  are the minimum and maximum of the  $x$  and  $y$  coordinates of particles inside the heap, respectively,  $n_x$  and  $n_y$  are the number of discretization intervals in the  $x$  and  $y$  directions,  $\Delta x$  and  $\Delta y$  are the distances between two adjacent sample points corresponding to  $x$  and  $y$  directions and  $h(x_i, y_i)$  is the height of the heap at the coordinate  $x_i, y_i$ . The choice of  $n_x$  and  $n_y$  is a trade-off between the numerical accuracy and the computational time. It should be high enough to mitigate the estimation error and as the same time it should be as low as possible for quick calculations and less consuming use of computer memory. In the present work,  $n_x$  and  $n_y$  were set to 10000. This number of sample points guarantees that each calculation takes only few seconds on a normal desktop computer and the results of bulk volume converge.

### 2.3.5. Ring shear tester simulations

The simulated geometry of a ring shear tester cell (Figure 6) is analogous to the experimental device described in Section 2.2.4. Previous research [57] has shown that the yield stress was independent of the shear cell size in simulations. However, a high particle-to-cell size ratio inside the shear cell could lead to erroneous values of the shear measurements [58], so the geometry was also scaled up by a  $SF = 4$ . A servo-control functionality of LIGGGHTS was applied to the top lid so the vertical component of the applied stress was continuously updated and maintained constant during the simulation. As in experiments, a pre-shear stage at  $\sigma_{pre} = 5$  kPa followed by a shear at  $\sigma = 2.5$  kPa was simulated. Shear stress is calculated from the  $\hat{x}$ -component of the torque exerted over the top lid surface as follows [41]:

$$\tau = \frac{M_D}{r_m A_D} \quad (16)$$

Where  $M_D$  is the torque acting during shear on the top of the lid,  $r_m = \left(\frac{2}{3}\right)(r_{out}^3 - r_{in}^3) / (r_{out}^2 - r_{in}^2)$  is the moment arm and  $A_D = \pi(r_{out}^2 - r_{in}^2)$  is the area of the lid, with and the outer  $r_{out}$  and inner  $r_{in}$  radii of the top lid, respectively. Other input parameters needed for the ring shear tester simulations are listed in *Table 4*.

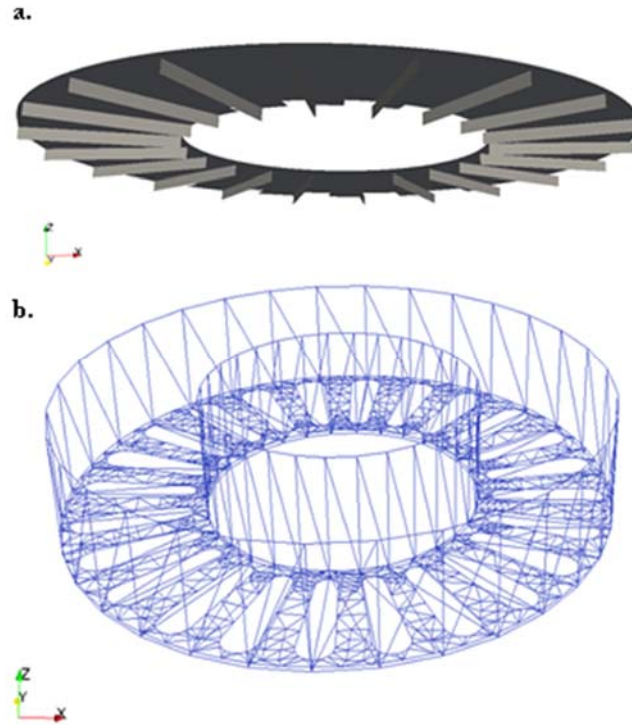


Figure 6. Geometry of the simulated ring shear tester. a. Top lid. b. Bottom cell.

## 2.4. Calibration approach

The flowchart of the calibration approach is presented in Figure 7. Regarding the choice of the parameters to be calibrated, a minimization of their number is desired since each additional parameter increases the complexity of the calibration. The previous research highlighted the high influence of the sliding and rolling friction coefficients on the angle-of-repose obtained in DEM simulations [19,22,59]. As the particle to wall interactions are very specific to each industrial or scientific problem, in this research only interparticle interaction parameters are calibrated: the sliding friction coefficient  $\mu_s$ , the rolling friction coefficient  $\mu_r$  and the cohesion energy density  $CED$ . All the other input values needed for the DEM model are shown in Table 4 and were set based on literature values for woody materials [6]. Preliminary simulations did not show significant effects of the particles' density on the AoR nor the void fraction inside the heap, so the value is set to  $1000 \text{ kg/m}^3$  for the fine samples in order to increase the time-step allowing stable simulations.

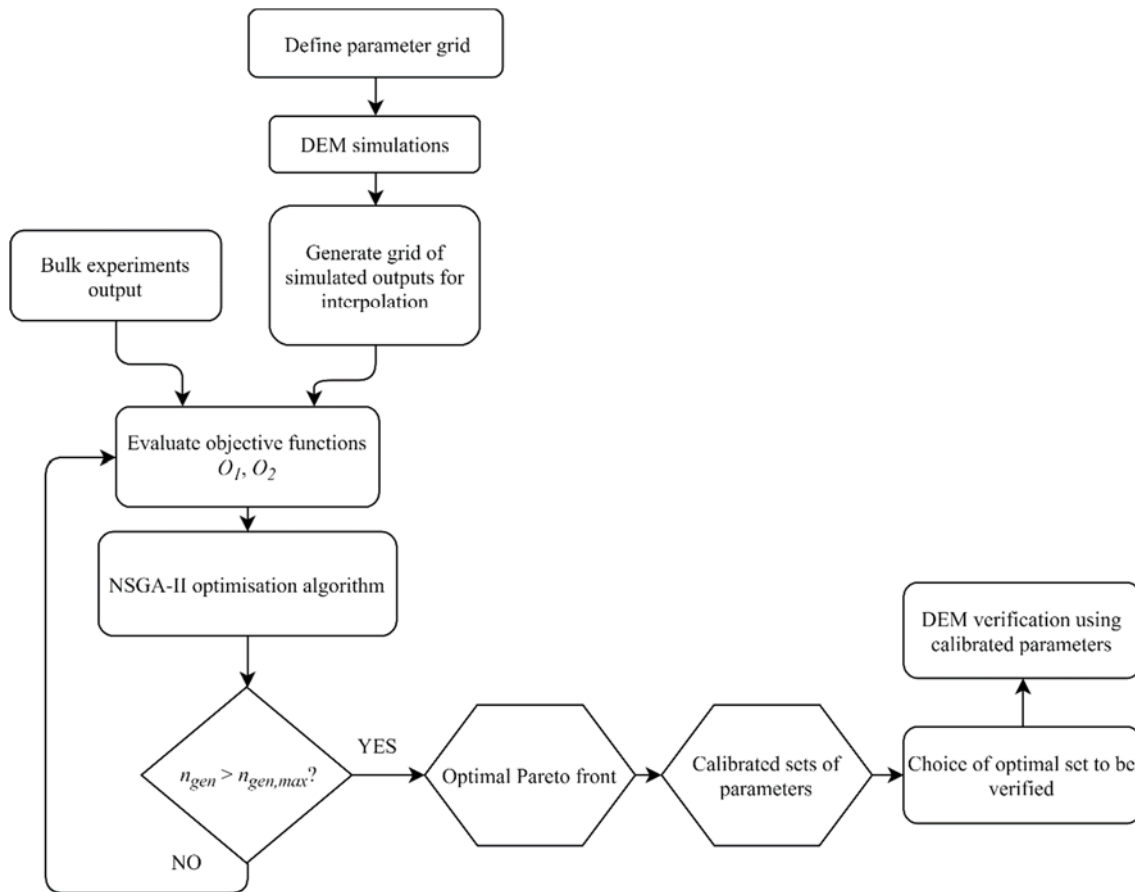


Figure 7. Flowchart of the calibration procedure.

#### 2.4.1. Selection and range of values of parameters to be calibrated

The tested values of each calibration parameter are shown in Table 5. If 5 values for each variable were to be tested,  $5^3 = 125$  simulations would be needed using a full factorial combination of variables. This is feasible in a practical time-frame for coarse samples (Sample 1) but for fine powders (Sample 2), even if using a coarse-graining approach, the high computation time required imposed a reduction of the number of values of the calibrated parameters from 5 to 3 (27 simulations). These values are the maximum, minimum and mean values written in bold type in Table 5. The full experimental plan of this work is presented in Appendix 1.

Table 4. DEM simulation parameters for particles and walls

Parameter	Sample 1	Sample 2
Poisson's ratio (particle-particle)		0.3
Poisson's ratio (particle-walls)		0.3
Particles density, kg/m <sup>3</sup>	350	1000
Young's modulus (particle-particle), Pa		5×10 <sup>6</sup>
Young's modulus (particle-wall), Pa		5×10 <sup>6</sup>
Coefficient of restitution (particle-particle)		0.1
Coefficient of restitution (particle-walls)		0.1
Coefficient of sliding friction (particle-steel)		0.4
Coefficient of sliding friction (particle-paper surface)		0.5
Coefficient of rolling friction (particle-walls)		0.5
Cohesion Energy Density (particle-walls), J/m <sup>3</sup>		0
Time-step (s)	1×10 <sup>-5</sup>	7×10 <sup>-6</sup>
Total number of particles (3 particles/clump)	10638	81309
Factory mass flow, heap AoR test, kg/s		5×10 <sup>-4</sup>
<b>Ring shear tester simulations</b>		
External radius, top lid, mm		127
Internal radius, top lid, mm		65
Depth, bottom cell, mm		52
Total number of particles (3 particles/clump)	15000	150000
Rotational speed, top lid, deg/s		18

Table 5. Set of calibration parameters tested.

Parameter	Variable values				
Coefficient of sliding friction ( $\mu_s$ )	<b>0.1</b>	0.3	<b>0.5</b>	0.7	<b>0.9</b>
Coefficient of rolling friction ( $\mu_r$ )	<b>0.1</b>	0.3	<b>0.5</b>	0.7	<b>0.9</b>
Cohesion Energy Density, $CED$ (J/m <sup>3</sup> )	<b>0</b>	10000	<b>20000</b>	50000	<b>80000</b>

## 2.5. Optimization problem setup (genetic algorithm)

The optimization was carried out using a multiobjective evolutionary algorithm (Non-dominated Sorting Genetic Algorithm II, NSGA-II) [60] proven successful for DEM calibration [24,25]. Input parameters for the genetic algorithm are listed in Table 6. By using 10 bits for encoding each calibration parameter, the number of possible values for each parameter is  $2^{10} = 1024$ . Since 3 parameters are being optimized, each “individual” in the population is encoded by a binary string of length 30 bits. This leads to the numerical precision listed in Table 6 for each parameter.

Table 6. Input parameters of NSGA-II

Population size	2000
Chromosome length (bit)	30
Maximum number of generations	100
Crossover probability	0.9
Mutation probability	0.01

Two specific objective functions were defined for the minimization of the discrepancy between numerical and experimental results. The first objective function  $O_1$  is defined as the total relative error between the simulation results and the experimental measurements of AoR and bulk density:

$$O_1 = \frac{|AoR_{ex} - AoR_{sim}|}{AoR_{ex}} + \frac{|\rho_{ex} - \rho_{sim}|}{\rho_{ex}} \quad (17)$$

In this optimization function, the weights of the two error components are equally contributing to the total simulation error.

The second objective function  $O_2$  is based on the rectangular container output and aims to reduce the difference between the simulated and the experimental  $p$  factor:

$$O_2 = \frac{|p_{ex} - p_{sim}|}{p_{ex}} \quad (18)$$

Table 7. Numerical precision of binary encoded factors.

Parameter	Interval	Numerical precision
$\mu_s$	[0.1, 0.9]	$7.81 \times 10^{-4}$
$\mu_r$	[0.1, 0.9]	$7.81 \times 10^{-4}$
CED	[0, 80000]	78.125

### 3. RESULTS AND DISCUSSION

#### 3.1. Bulk behavior tests

##### 3.1.1. Bulk density

The experimental results in the Table 8 show an effect of particle characteristics on bulk density of the samples. Interestingly, regarding the particle size, smaller values of bulk density were systematically found for powders with the lowest granulometry. Finer samples had a bulk density 10 % lower than coarse samples. When dealing with non-cohesive materials, a better spatial arrangement of particles is obtained for finer particles so, generally, a decrease of particle size is accompanied by an increase in bulk density. The opposite trend observed for biomass samples would be due to cohesion effects: the presence of fine cohesive particles creates bigger void spaces which reduces bulk density. Similar results were observed by Mani et al. [61] for wheat and barley straws, corn stover and switchgrass samples.

### 3.1.2. Angle of Repose tests

The mean values of the angles of repose are reported in Table 8. The values of the standard deviation are also reported and show that error was always below 4 %, meaning a relatively good reproducibility.

There is an obvious effect of the sample characteristics on the AoR of the heaps formed. The finer sieving cut (sample 2) formed steeper heaps with values of AoR 67 % greater than the coarse cut (sample 1).

Table 8. Bulk behavior experiments results (standard deviation is reported in parentheses).

Sample	1 (Coarse sieving cut)	2 (Fine sieve cut)
$\rho_b$ (kg/m <sup>3</sup> )	184.2 (5.7)	165.6 (5.1)
AoR (°)	27.7 (0.7)	46.3 (1.6)

Following the classification criteria based on the AoR established by Ileji et al. [62] for lignocellulosic plant biomass, coarse poplar powders could be classified as free flowing, while fine powders are rather poor flowing.

### 3.1.3. Rectangular container test

No biomass particles were observed to flow when the lid of the rectangular container was lifted. Indeed, very stable stacks of particles were formed for all the samples. This is the result of the combined effect of particles shape and size that trigger interlocking and interparticle cohesive forces. As result of this, the retainment ratio  $P$  (Eq. 3) was found to be 1 for both samples.

## 3.2. DEM simulations

Figure 8 shows some typical heaps and rectangular containers obtained by DEM modelling for both samples, along with the values of the calibration parameters used. Visually, the effect of modifying contact model parameters is evident. The situations represented on the left side of the Figure 8 show a material with a rather free flowing behavior, while images on the right side of Figure 8 represent rather a very cohesive behavior, with greater angles of repose and the formation of a stable stack of particles inside a container.

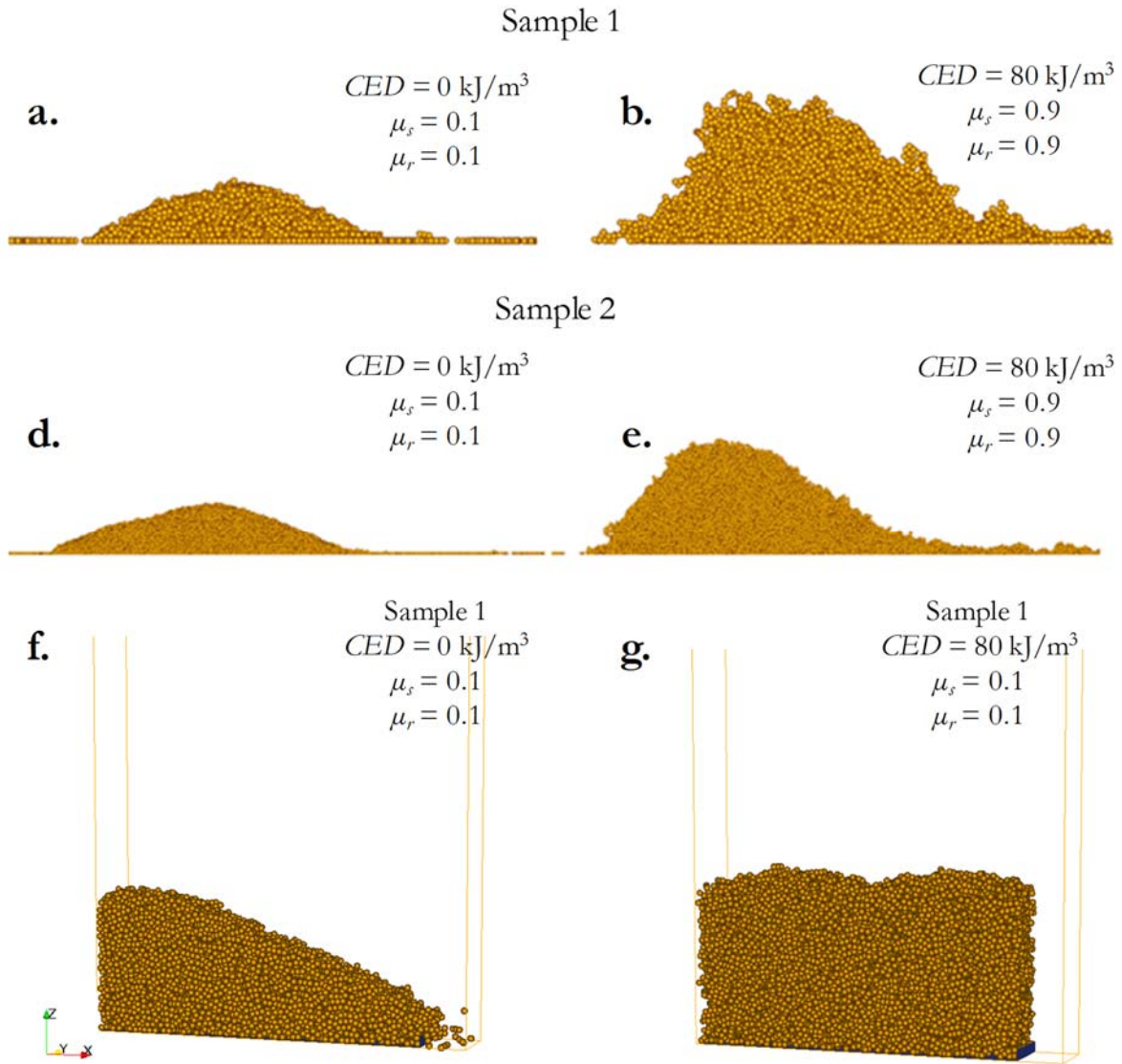


Figure 8. Examples of heaps obtained and rectangular container test from DEM simulations.

### 3.2.1. Pareto chart analysis

Determining if variation of DEM parameters produce discriminative effects in bulk responses is important to reduce the number of calibration inputs. For this purpose, a statistical analysis using Pareto charts was used in this work.

A Pareto chart allows to compare the relative magnitude and the statistical significance of effects of tested variables on the measured responses. Details on the elaboration and interpretation of the Pareto charts can be found in [63].



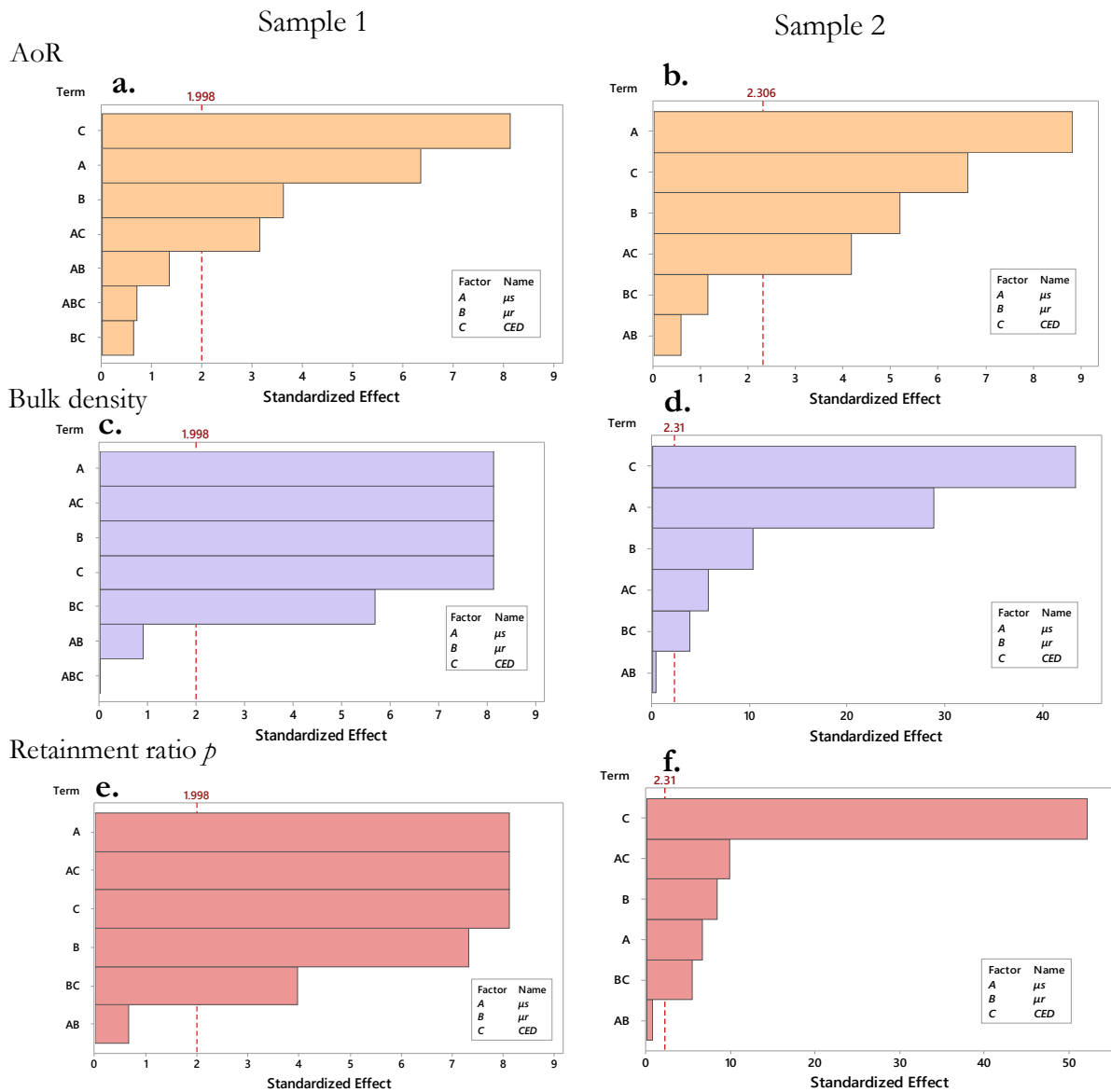


Figure 9. Pareto charts of the standardized effects.

For the coarse samples, the *CED* has the biggest effect on the values of AoR (Figure 9a). In a lower degree, sliding friction, rolling friction and the combined effect of sliding friction and *CED* also influenced the AoR. In the case of the bulk density (Figure 9c), all the 3 factors seem to have the same level of influence on the response, as well as the combined effects of  $\mu_s$ -*CED*. Regarding the retainment ratio, although *CED* and  $\mu_s$  and their interactions had the greater effect, rolling friction also played a role in controlling the number of particles remaining in the container after the lid is opened (Figure 9c).

For the fines sample, *CED* was the predominant influential factor for both bulk density and *p* ratio responses (Figure 9b,d), while in the case of AoR,  $\mu_s$  had a greater effect (Figure 9f).

These results suggest that the three chosen calibration parameters were important in controlling the measured responses and determined the main effects that influence the system. In addition, the relative effects were different depending on the analyzed response. Therefore, their calibration is required.

### 3.2.2. *Heap angle of repose and bulk density*

Figure 10 and Figure 11 show 2D contour surface representations of the effects of the calibration parameters on the AoR, the bulk density and the retainment ratio  $p$ . For clarity reasons, only surfaces for  $CED = 0, 20$  and  $80 \text{ kJ/m}^3$  are presented. Contour surfaces of the  $p$  ratio for  $CED = 80 \text{ kJ/m}^3$  are not shown as all simulations led to  $p \approx 1$ , regardless of  $\mu_s$  and  $\mu_r$  values. These representations clearly show the coupled effects that sliding and rolling friction coefficients as well as cohesion have on the three responses analyzed.

From the contours of Figure 10 it is noticeable that a single value of the bulk responses can be achieved from a wide range of parameters (each contour line spans over a wide range of both sliding and rolling friction coefficients and the same colors in the color scale can be found in two or more different graphs). This highlights the importance of choosing enough bulk setups and responses for a robust DEM calibration.

In the case of the AoR response, changing cohesion level affects the trends of the surfaces, showing that effects of  $\mu_s$  and  $\mu_r$  are dependent on each other but also on  $CED$  magnitude. This is especially noticeable for the highest values of  $CED$ . For non-cohesive simulations (Figure 10a), rolling friction effects are more important when sliding friction is increased, and maximum values of AoR are attained for the highest values of  $\mu_s$  and  $\mu_r$ . This is in agreement with previous results by Wensrich and Katterfeld [64] who stated that the only way in which a large angle of repose could be achieved was if both of these mechanisms (rolling and sliding) worked together. However, interestingly, when cohesion is included, even if AoR tends to increase with increase in  $\mu_s$  and  $\mu_r$  values, maximum AoR values do not necessarily correspond to the highest values of  $\mu_s$  and  $\mu_r$ ; instead, they are located at intermedium values of  $\mu_s$  and  $\mu_r$ . Figure 10c shows that effects of rolling and sliding friction follow a less monotonous trend when  $CED$  is  $80 \text{ kJ/m}^3$ . A reason for this is that, for values of  $CED$  over  $50 \text{ kJ/m}^3$ , particles flowing over the conveyor tend to form relatively stable agglomerates that are spread over the heap's surface, forming heaps with a rougher and more irregular surface (Figure 8b). Therefore, AoR determination for very cohesive simulations could lead to values with

higher uncertainty as heap profiles are less well-described by linear regressions. This can be quantified through the calculation of the average coefficient of determination ( $r^2$ ) as function of the *CED* values (Figure 12). Indeed, a downward trend which is more marked for the sample 1 (coarse particles) than for sample 2 (fine particles) was observed.

As for the AoR, effects of calibration parameters on bulk density go hand-in-hand. Bulk density decreases when friction and cohesion are increased or when the rolling is more restricted (so a less “spherical behavior”). This is the result of a higher void created between particles when normal forces are allowed to dissipate to a bigger extent through bigger  $\mu_s$  values. Increasing the rolling resistance and cohesion also prevent particulates from finding a more compact spatial arrangement, so void fraction could be reduced. Bulk density seems to be sliding dominated for the values on top left of the contour figures ( $\mu_s < 0.3$ ) and rolling dominated for the values at the bottom right corner on those representations. This accentuates when cohesion is increased.

For sample 1, experimental values of AoR and bulk density (AoR = 27.7°,  $\rho_b = 184.2 \text{ kg/m}^3$ ) can only be found for the lower values of cohesion, but a high  $p$  ratio needs a high value of *CED*. Thus, a trade-off through optimization has to be found.

Regarding sample 2, small effects of cohesion on the AoR were found within the range 0 to 20 kJ/m<sup>3</sup>. Unlike sample 1, a more gradual increase of AoR with rolling resistance increase was found for *CED* = 80 kJ/m<sup>3</sup>. Regarding bulk density, similar trends were found between both samples. Target values (AoR = 46.3°,  $\rho_b = 165.6 \text{ kg/m}^3$ ) can be found on Figure 11c and Figure 11e, but as for sample 1, a  $p$  value of 1 is only possible for the most cohesive sets of simulations.

Sample 1

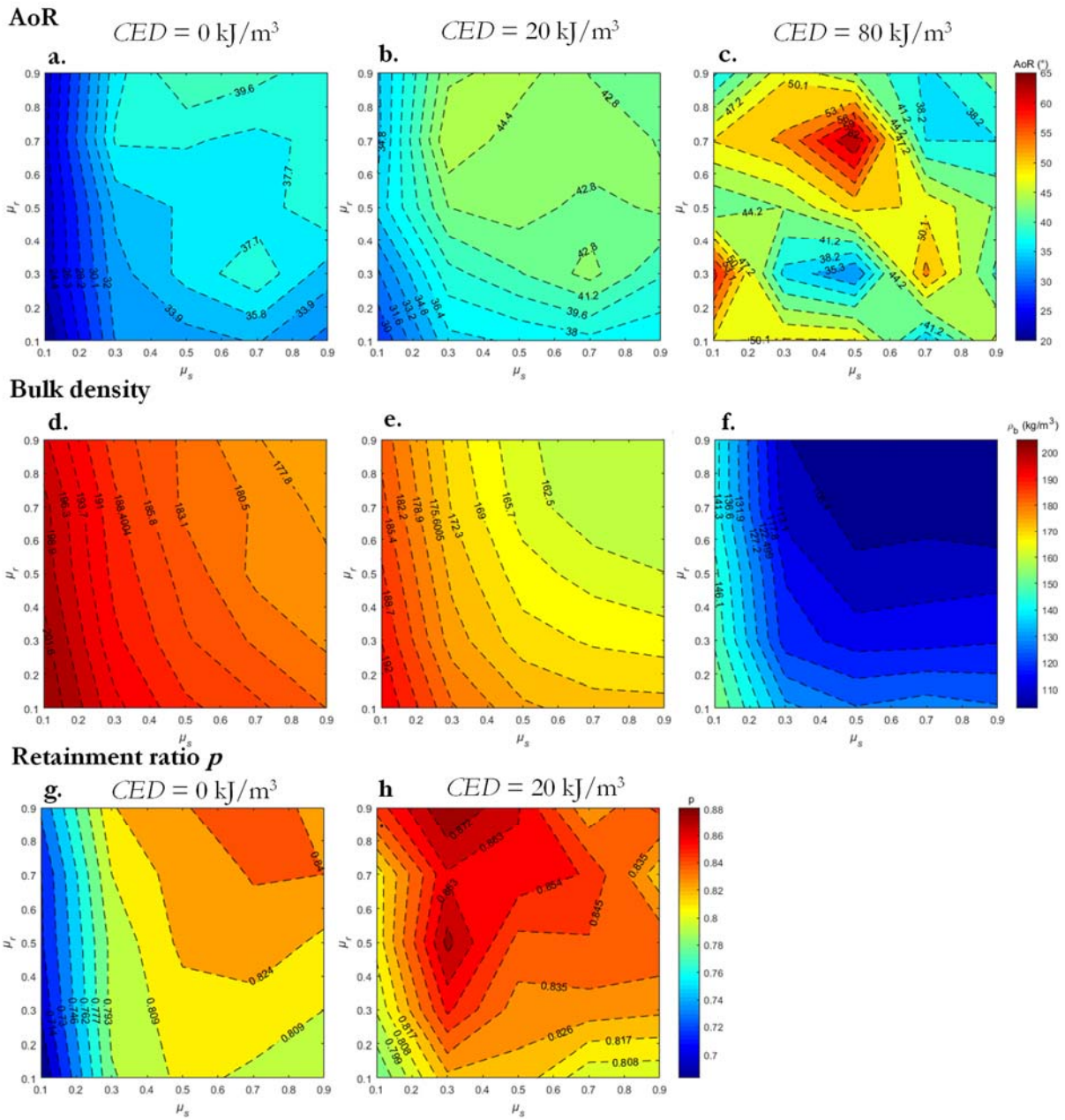


Figure 10. Contour surface responses for sample 1.

In order to reach values of  $p$  ratio close to 1, a particle's shape representation that strengthens particles spatial interlocking could reduce the need for high  $CED$  values (e.g. through non-axial or hooked shapes). Nevertheless, this would typically require a particle's model including more spheres per clump, as well as a highly polydisperse system, which would reduce simulation performances beyond a practical interest.

Globally, when comparing simulations for samples 1 and 2 with low-mid cohesion, relatively similar values of AoR and bulk density were found for the two samples when calibration parameters were the same. On the contrary, the experimental results for samples 1 and 2 were significantly different.

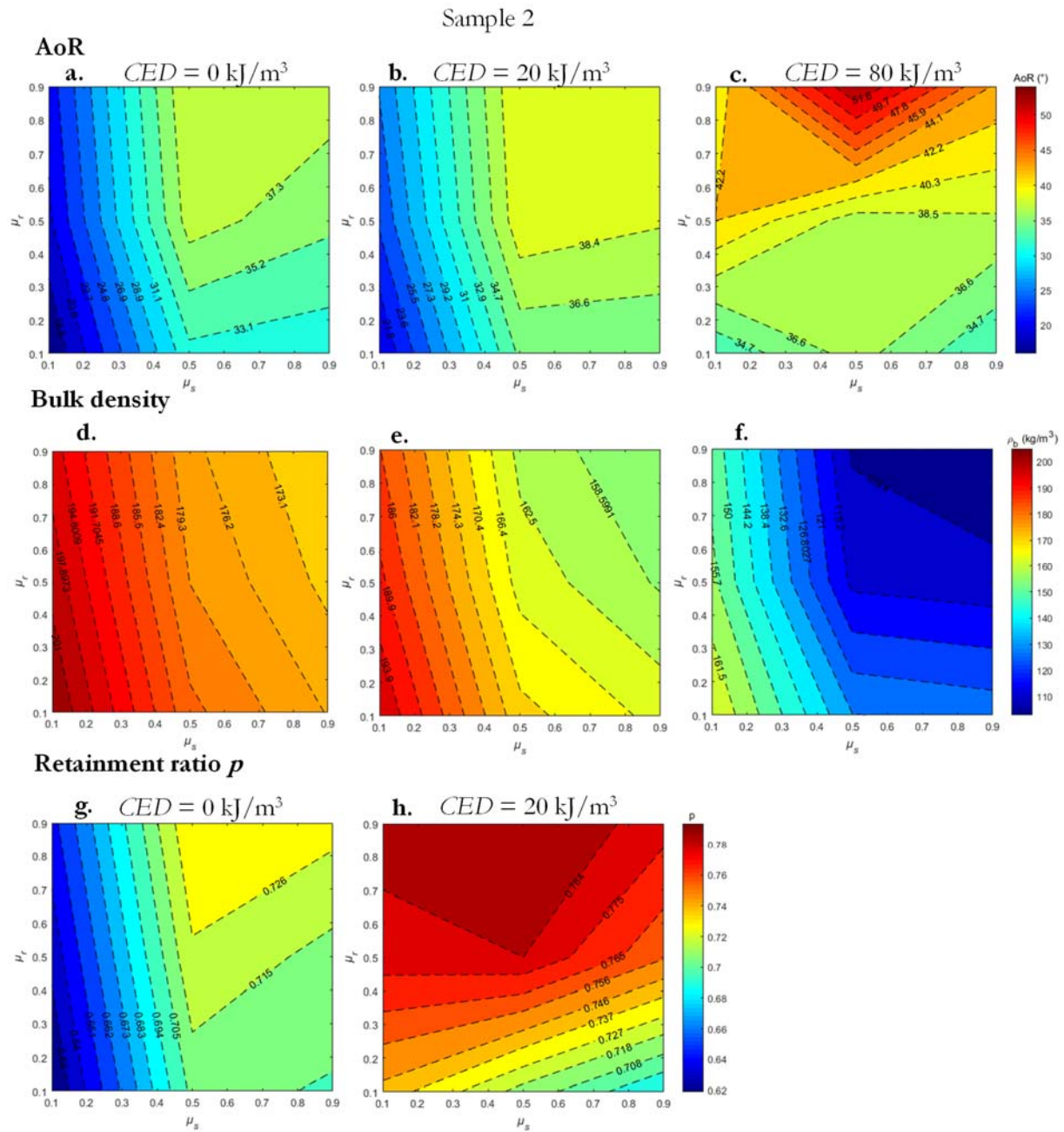


Figure 11. Contour surface responses for sample 2.

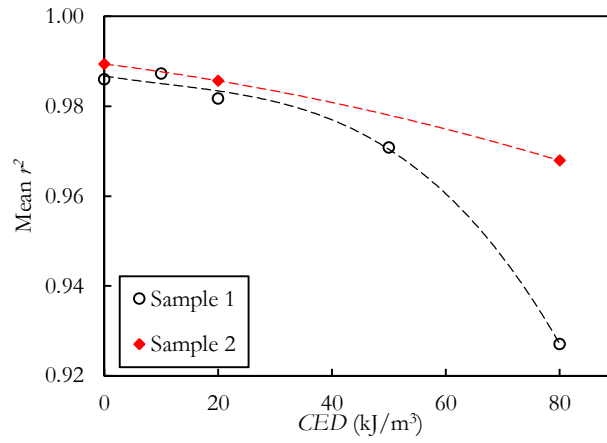


Figure 12. Average coefficients of determination of heaps profiles.

### 3.2.3. Main effects of calibrated parameters

Using MINITAB's tool for analysis of factorial designs [65], the main effects plots presented in Figure 13 were obtained. These plots are useful for quantitatively assessing the influence of each level of  $\mu_s$ ,  $\mu_r$  and  $CED$  on the mean responses of AoR, bulk density and  $p$  ratio.

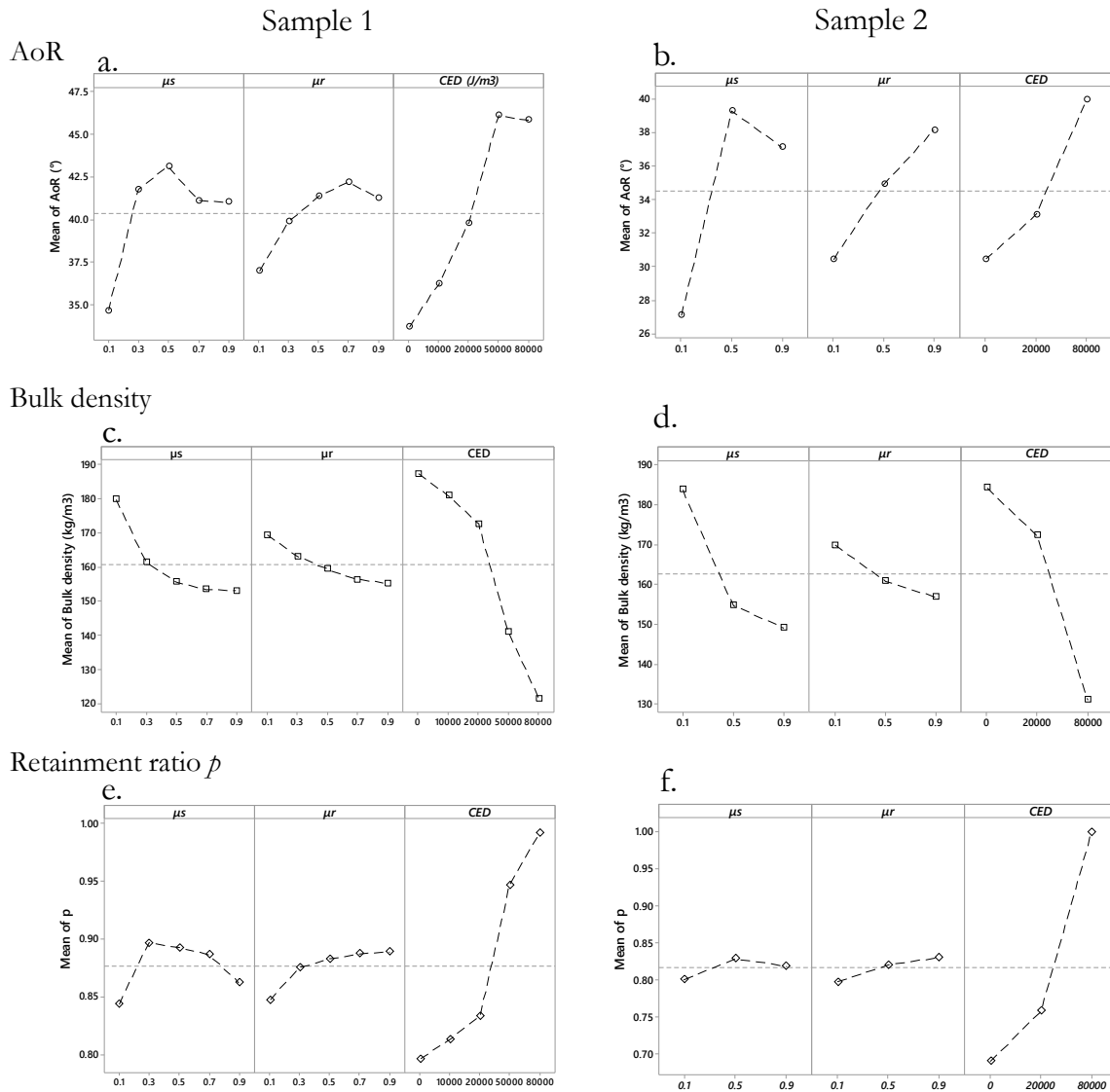


Figure 13. Main effects plots. The dotted horizontal line represents the overall mean.

Globally, similar trends were found for both samples, both qualitatively and quantitatively, with a greater resolution for sample 1 than that for sample 2 as more parameters values could be tested. In the case of the coarse sample 1, a sharp increase (21%) of AoR was observed as  $\mu_s$  increased from 0.1 to 0.3. In average, higher values of AoR were obtained for  $\mu_s = 0.5$ . Sliding friction governs the translational motion of the particles by defining the magnitude of normal force that it is dissipated as a tangential component. This means that a large sliding friction coefficient can tolerate a large magnitude of the elastic deformation in the tangential direction and enhance the stability of the individual contacts amongst particles. However, sliding friction defines only a truncation parameter of the tangential force and not its absolute value when the truncation criteria is not met. This could explain the important gap of AoR observed when  $\mu_s$  is increased

from 0.1 to 0.3 and the low AoR variation when  $\mu_s$  is increased above 0.3. For very low values of  $\mu_s$  the tangential displacement is highly constrained and corresponds to the value defined by the product of  $\mu_s$  and the normal force on particles (Coulomb's friction limit). For higher values of  $\mu_s$  the probability of normal forces exceeding the truncation criteria is reduced and therefore further increase of  $\mu_s$  would have a lower effect on the variation of the tangential dissipation and therefore on the angle of repose.

Increasing rolling friction from  $\mu_r = 0.1$  to  $\mu_r = 0.7$  gradually increased the mean AoR by +15 % as shown in Figure 13a. A large rolling friction coefficient means a large resistance force to the rotational movement of the spheres clump, which provides an effective mechanism to consume the kinetic energy and reduce the rotational motion, leading to the formation of heaps with higher potentials and AoR [66].

The greatest variation of AoR was observed when the *CED* effect is analyzed: AoR below 35° were obtained for non-cohesive simulations while the highest values of *CED* led to AoR over 46° (+36 %).

Regarding bulk density, the downward trends of Figure 13c-d summarize the observations made for the contour surfaces presented in section 3.2.2. The increase of sliding and rolling friction coefficients triggered a less compacted settlement of particles inside the heap, thus creating more void spaces and reducing bulk density. For values of  $\mu_s, \mu_r > 0.7$  bulk density seems to reach a low plateau. As for *CED* effect, an important decrease of  $\rho_b$  by 36% and 30% for sample 1 and sample 2 respectively was observed when non-cohesive and highly cohesive simulations ( $CED = 80 \text{ kJ/m}^3$ ) are compared.

For both samples, there is a peak of *P* ratio when varying  $\mu_s$  values from 0.1 to 0.9. Interestingly, in the case of the coarse sample, increasing sliding friction coefficient to 0.9 lead to much more particles flowing out of the container. This is probably because when increasing friction, particles at the border of the stack are more likely to be dragged by particles flowing out the silo, which, together with the effects of cohesion, will lead to smaller values of the retainment ratio. For  $CED = 80 \text{ kJ/m}^3$ , however, cohesion is strong enough to hold particles together and conceal the effects of  $\mu_s$  or  $\mu_r$ .

For both samples, limiting particles rotation tended to generate more stable stacks as can be seen from the slight increase of the *P* ratio with increase of  $\mu_r$ . Finally, increasing values of the *CED* was directly related with the number of particles staying in the container after the lid was opened. Among the variables studied,



*CED* increase is therefore the best approach to simulate particle interlocking and to numerically reproduce the particles cohesion observed in experiments.

### 3.3. Calibration and selection of optimal values

#### 3.3.1. Pareto fronts, 3D representation of optimal values

The evolution of the two objective functions for sample 1 over 100 generations are shown in the Figure 14. The 2000 individuals constituting the initial population are spread over a relatively wide range of the objective function values that gradually narrows with successive iterations. The number of individuals stay constant, so the Pareto fronts shrink around the optimal values with the evolution of the population. Through the iteration process, the fronts converged to an optimum where no further improvement was observed in succeeding generations. For both samples, a convergent front was obtained from the 50th generation.

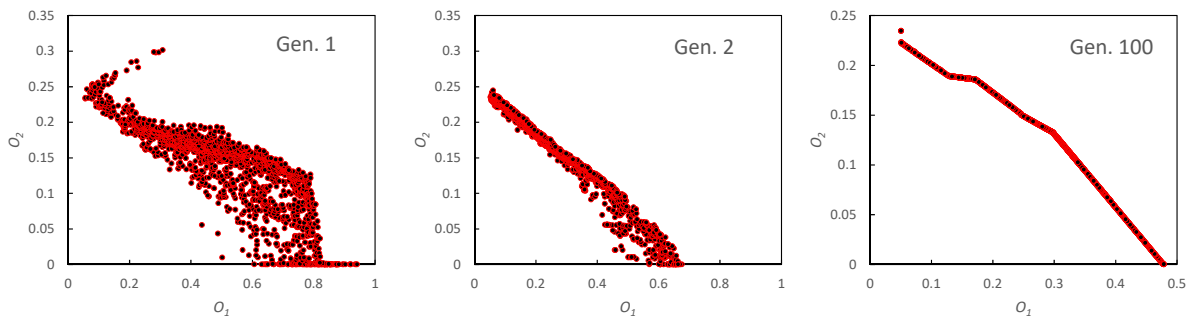


Figure 14. Pareto front evolution over 100 generations of NSGA-II optimization.

As observed through the Pareto fronts, multiobjective optimizations lead to results in which trade-offs between the objective functions were encountered. The optimal solutions that allowed to obtain values of AoR and bulk density closer to the experimental measurements yielded low  $p$  values and vice versa. In order to have a comprehensive view of the sets of calibrated parameters that better adjust the bulk experimental properties of each sample, the optimal values for the last generation of NSGA-II optimizations are presented in Figure 15. A color and size scale were used to highlight the values of the total error, calculated as the sum of the values of the objective functions  $O_1 + O_2$ . For sample 1, sets of optimal calibration parameters with a relatively broad range of solutions were obtained, especially for *CED* values which could vary between 10 and 50 kJ/m<sup>3</sup>. For sample 2, a narrower range of optimal sets is shown in

Figure 15. The solutions giving the lowest value of  $O_1 + O_2$  were input in the LIGGGHTS program and the simulation results are presented and compared against the experimental values in Table 9.

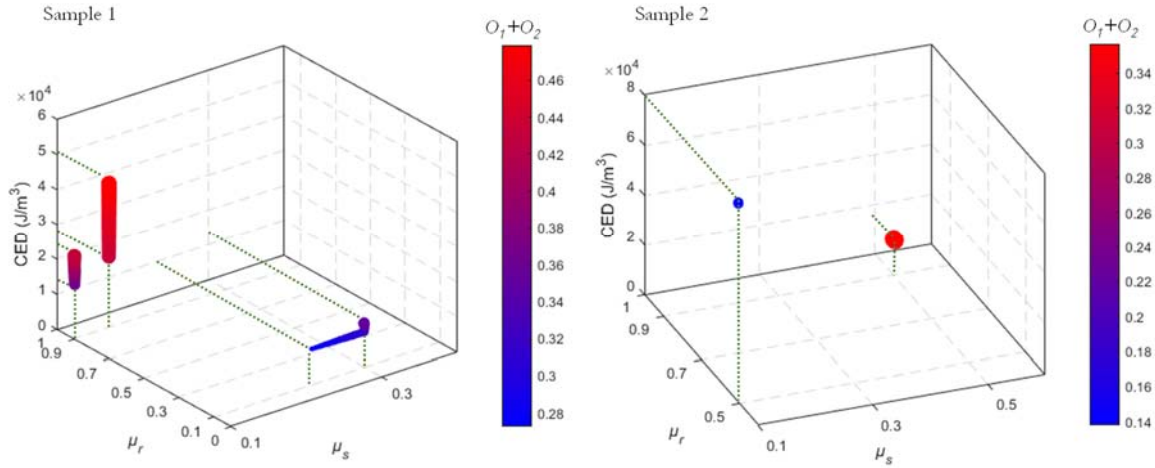


Figure 15. Sets of optimal calibrated parameters for sample 1 and 2. Size and color scale indicate the sum of  $O_1 + O_2$  values corresponding to each set of  $\mu_s$ ,  $\mu_r$  and  $CED$ .

The calibrations based exclusively on the angle of repose and the bulk density would not lead to a material having enough interparticle cohesion to hold particles together inside a container. Therefore, including the rectangular container test as a bulk response for calibration was decisive to expose the cohesive character of biomass particles. Incorporating the retainment ratio response adds a cohesive feature to the material that could more realistically simulate blocking problems on feed systems for biomass particles. Additionally, calibration using the  $p$  ratio sensibly reduced the diversity of the optimal values of  $\mu_s$ ,  $\mu_r$  and  $CED$ . Thus, it is clear that separate calibration test from different macroscopic responses can yield different results and that calibration based on a large number of parameters and bulk responses is preferable.

Table 9. Optimized values of  $\mu_s$ ,  $\mu_r$  and  $CED$  and comparison of simulated responses (Sim.) against experimental measurements (Exp.).  $e$ : relative error between experimental and DEM responses.

Sample	$\mu_s$	$\mu_r$	$CED$ (kJ/m <sup>3</sup> )	$O_1 + O_2$	$AoR$ (°)			$\rho_b$ (kg/m <sup>3</sup> )			$p$		
					Sim.	Exp.	$e$ (%)	Sim.	Exp.	$e$ (%)	Sim.	Exp.	$e$ (%)
1	0.2298	0.1000	10.01	0.27	30.0	27.7	8.3	192.2	184.2	4.3	0.80	1	20.0
2	0.1000	0.5004	80.00	0.17	42.3	46.3	8.7	157.1	165.6	5.1	1.00	1	0.0

From Table 9 it can be seen that there was little discrepancy between the simulated and the experimental AoR, bulk density and  $p$  ratio for both samples. In the case of sample 1, even if the AoR and bulk density values were better adjusted than those of sample 2, optimization led to particles without enough cohesive strength to form a stable stack in the rectangular container simulations. The optimized values of  $CED$  reflect a much more cohesive behavior for finer samples, which corresponds to the experimental observations.

### 3.3.2. Ring shear tester simulations

Values presented in Table 9 were used to simulate a shear sequence in a ring shear tester. Figure 16 compares the simulation results against the experimental evolution of shear stress. Two shear cycles are represented, starting by a preshear step at  $\sigma_{pre} = 5$  kPa and followed by a shear at  $\sigma_{sb} = 2.5$  kPa. This preshear-shear sequence is repeated for  $\sigma_{sb} = 3.75$  kPa. Stresses are plotted against rotation angle defined as the product of time and shear velocity. Although simulation results are relatively noisy (due to the scaled particles and the oscillation of the servo-controlled normal force), it is encouraging that simulation results for sample 1 were very close to experimental shear stress profiles in terms of evolution of the curve shape and the average yield stresses.

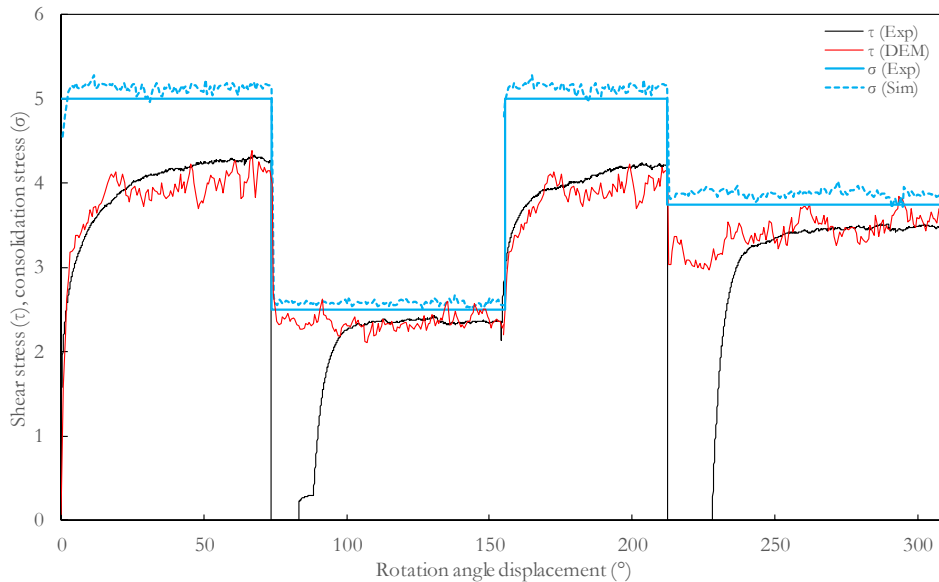


Figure 16. Simulated (DEM) and experimental (Exp) evolution of shear ( $\tau$ ) and consolidation stresses ( $\sigma$ ) for sample 1.

Yield stresses of preshear and shear for both samples are listed in Table 10. Values of shear stress were slightly underestimated in DEM simulations for sample 1. A greater gap between the experimental and

simulations results was yet observed for sample 2. This can be related to the fact that responses shown in Section 3.3.1 for sample 2 were less well predicted using the calibrated parameters than those of coarse powders.

Table 10. Simulation (Sim.) and experimental (Exp.) results for ring shear tester tests.

	Preshear stress at $\sigma_{presb} = 5$ kPa			Shear stress at $\sigma_{sb} = 2.5$ kPa		
	Exp.	Sim.	$e$ (%)	Exp.	Sim.	$e$ (%)
Sample 1	4.31	3.94	8.6	2.45	2.32	5.3
Sample 2	4.81	3.49	27.4	2.87	2.51	12.5

The under-estimation of the experimental results from simulations for sample 2 shows that these results should be treated with caution. Indeed, as highlighted by [67], calibration should take into account the nature of the actual simulated process. Calibration using angle of repose, bulk density and shear box tests might therefore not be sufficient for simulation of materials under a consolidated state, as is the case in shear testers. Furthermore, the use of JKR cohesion models has recently been shown not to adequately capture the stress behavior of some cohesive powders, particularly at relatively high consolidation stresses [68]. This has led to the development of new cohesion contact models that consider contact plasticity. Additional work will therefore evaluate the relevance of JKR models compared to cohesive elasto-plastic models for biomass particles.

#### 4. CONCLUSION

Biomass powders characteristics – such as small particles size, cohesive behavior, low particle density and elongated shape – make bulk simulations highly challenging considering the current DEM state of development. This work aimed at producing a realistic, calibrated and efficient material model for lignocellulosic biomass powders to be eventually used in feeding systems for entrained-flow gasification. We successfully developed a DEM material model for biomass powders by using a coarse-grained multisphere representation of shape and size distributions of particles along with a Hertz-Mindlin-EPDS2-SJKR cohesive force model.

The application of a calibration procedure that uses a NSGA-II optimization algorithm was successful in determining the coefficients of sliding friction, rolling friction and a cohesive energy density term for two

biomass powder populations: a coarse sieving cut between 500  $\mu\text{m}$  and 710  $\mu\text{m}$ , and a fine cut between 200 and 315  $\mu\text{m}$ . The results presented here showed that the calibrated contact-law parameters fitted the physical responses accurately, and a validation using a ring shear tester showed promising results. The application of a typically used trial-and-error approach for calibration would have been highly time-consuming compared to the systematic approach used in this work.

This research highlighted the importance of adequately selecting bulk experiments for calibration: only taking results from angle-of-repose and bulk density measurements would not replicate the cohesive behavior of biomass particles to their actual extent. Including additional bulk responses such as a rectangular container test (shear box) reduced the diversity of optimal calibrated parameters and allowed to obtain a material model that represents better blocking problems in feeding systems.

With the aim of improving the predictive capability of the DEM model for biomass powders, future research could include additional bulk setups that discriminate between different cohesive strengths of biomass powders, as well as validation under a variety of stress and flow conditions.

The findings presented here showed a scale-dependency of the simulations for the AoR test. The prospect of being able to apply at an industrial scale the calibrated parameters found using the framework described here serves as a stimulus for future research on the scalability of the calibration setups. This remains an important issue to be addressed in future studies, especially regarding cohesive and elongated materials such as biomass particles. Future work should also address the relevance of using flexible particle models that might be more suitable for biomass particles.

## Acknowledgements

The authors would like to acknowledge the Ministry of Higher Education and Research of France as well as the French-Dutch Network (Eole Scholarship) for their financial support. John Pachón-Morales is also grateful to the section Transport Engineering and Logistics of Delft University of Technology, where a part of the presented work was conducted. We are especially thankful to the French Council for Poplar (CNP) and the sawmill Huberlant (Cormicy, France) for kindly providing the wood used in this work.

## Appendix A. Experimental plan

The Table A-1 contains the experimental plan used in this work.

Table A-1. Experimental plan of this work.

Sample 1				Sample 2											
Run N°	$\mu_s$	$\mu_r$	$CED$ (kJ/m <sup>3</sup> )	Run N°	$\mu_s$	$\mu_r$	$CED$ (kJ/m <sup>3</sup> )	Run N°	$\mu_s$	$\mu_r$	$CED$ (kJ/m <sup>3</sup> )	Run N°	$\mu_s$	$\mu_r$	$CED$ (kJ/m <sup>3</sup> )
1	0.1	0.1	0	43	0.5	0.7	10	85	0.9	0.3	50	1	0.1	0.1	0
2	0.3	0.1	0	44	0.7	0.7	10	86	0.1	0.5	50	2	0.5	0.1	0
3	0.5	0.1	0	45	0.9	0.7	10	87	0.3	0.5	50	3	0.9	0.1	0
4	0.7	0.1	0	46	0.1	0.9	10	88	0.5	0.5	50	4	0.1	0.5	0
5	0.9	0.1	0	47	0.3	0.9	10	89	0.7	0.5	50	5	0.5	0.5	0
6	0.1	0.3	0	48	0.5	0.9	10	90	0.9	0.5	50	6	0.9	0.5	0
7	0.3	0.3	0	49	0.7	0.9	10	91	0.1	0.7	50	7	0.1	0.9	0
8	0.5	0.3	0	50	0.9	0.9	10	92	0.3	0.7	50	8	0.5	0.9	0
9	0.7	0.3	0	51	0.1	0.1	20	93	0.5	0.7	50	9	0.9	0.9	0
10	0.9	0.3	0	52	0.3	0.1	20	94	0.7	0.7	50	10	0.1	0.1	20
11	0.1	0.5	0	53	0.5	0.1	20	95	0.9	0.7	50	11	0.5	0.1	20
12	0.3	0.5	0	54	0.7	0.1	20	96	0.1	0.9	50	12	0.9	0.1	20
13	0.5	0.5	0	55	0.9	0.1	20	97	0.3	0.9	50	13	0.1	0.5	20
14	0.7	0.5	0	56	0.1	0.3	20	98	0.5	0.9	50	14	0.5	0.5	20
15	0.9	0.5	0	57	0.3	0.3	20	99	0.7	0.9	50	15	0.9	0.5	20
16	0.1	0.7	0	58	0.5	0.3	20	100	0.9	0.9	50	16	0.1	0.9	20
17	0.3	0.7	0	59	0.7	0.3	20	101	0.1	0.1	80	17	0.5	0.9	20
18	0.5	0.7	0	60	0.9	0.3	20	102	0.3	0.1	80	18	0.9	0.9	20
19	0.7	0.7	0	61	0.1	0.5	20	103	0.5	0.1	80	19	0.1	0.1	80
20	0.9	0.7	0	62	0.3	0.5	20	104	0.7	0.1	80	20	0.5	0.1	80
21	0.1	0.9	0	63	0.5	0.5	20	105	0.9	0.1	80	21	0.9	0.1	80
22	0.3	0.9	0	64	0.7	0.5	20	106	0.1	0.3	80	22	0.1	0.5	80
23	0.5	0.9	0	65	0.9	0.5	20	107	0.3	0.3	80	23	0.5	0.5	80
24	0.7	0.9	0	66	0.1	0.7	20	108	0.5	0.3	80	24	0.9	0.5	80
25	0.9	0.9	0	67	0.3	0.7	20	109	0.7	0.3	80	25	0.1	0.9	80
26	0.1	0.1	10	68	0.5	0.7	20	110	0.9	0.3	80	26	0.5	0.9	80
27	0.3	0.1	10	69	0.7	0.7	20	111	0.1	0.5	80	27	0.9	0.9	80
28	0.5	0.1	10	70	0.9	0.7	20	112	0.3	0.5	80				
29	0.7	0.1	10	71	0.1	0.9	20	113	0.5	0.5	80				
30	0.9	0.1	10	72	0.3	0.9	20	114	0.7	0.5	80				
31	0.1	0.3	10	73	0.5	0.9	20	115	0.9	0.5	80				
32	0.3	0.3	10	74	0.7	0.9	20	116	0.1	0.7	80				
33	0.5	0.3	10	75	0.9	0.9	20	117	0.3	0.7	80				
34	0.7	0.3	10	76	0.1	0.1	50	118	0.5	0.7	80				
35	0.9	0.3	10	77	0.3	0.1	50	119	0.7	0.7	80				
36	0.1	0.5	10	78	0.5	0.1	50	120	0.9	0.7	80				
37	0.3	0.5	10	79	0.7	0.1	50	121	0.1	0.9	80				
38	0.5	0.5	10	80	0.9	0.1	50	122	0.3	0.9	80				
39	0.7	0.5	10	81	0.1	0.3	50	123	0.5	0.9	80				
40	0.9	0.5	10	82	0.3	0.3	50	124	0.7	0.9	80				
41	0.1	0.7	10	83	0.5	0.3	50	125	0.9	0.9	80				
42	0.3	0.7	10	84	0.7	0.3	50								

## Appendix B. Individual simulation results

Figure 17 shows the totality of results from simulations. Each run number corresponds to a set of  $\mu_s$ ,  $\mu_r$  and  $CED$  values.

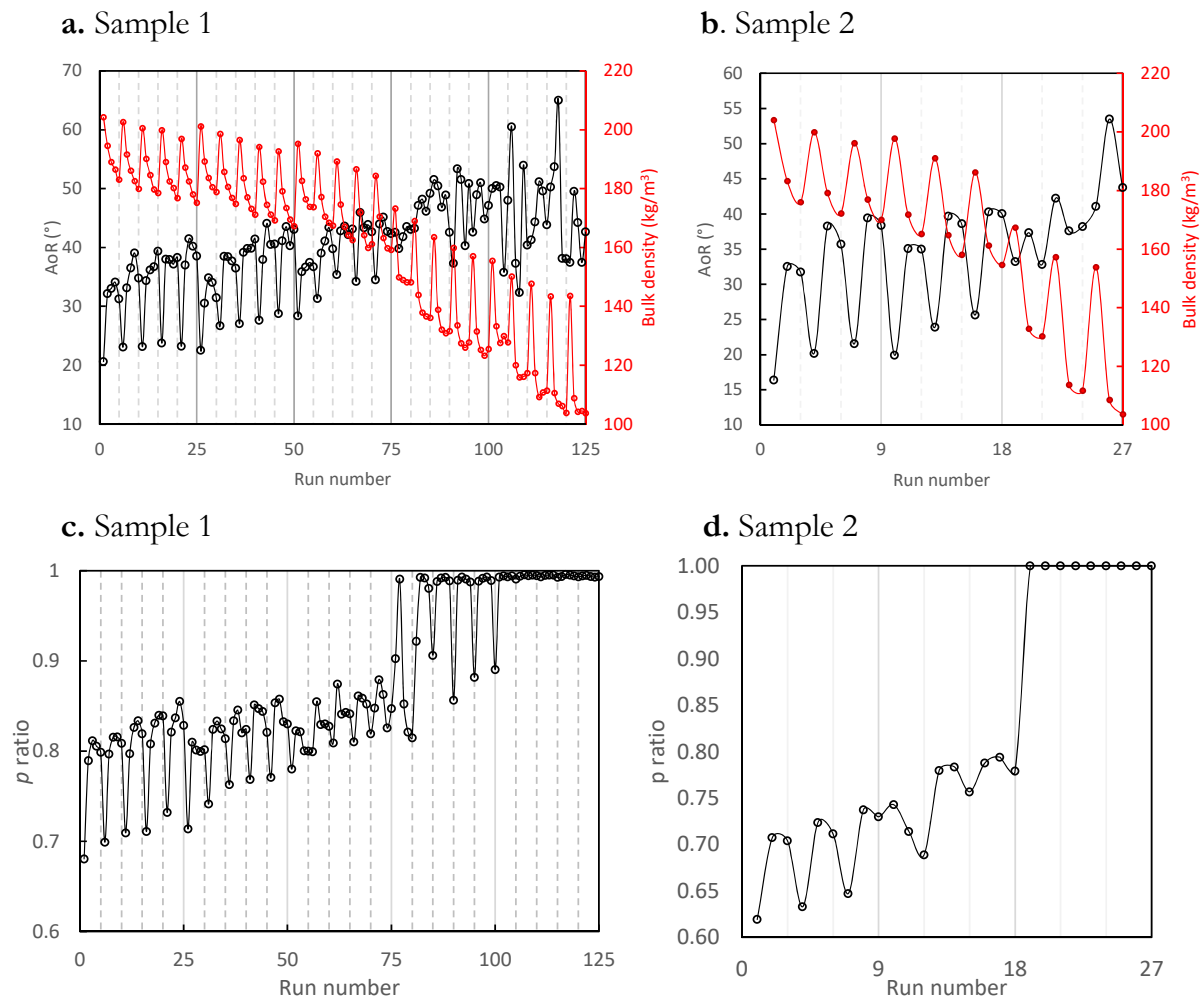


Figure 17. Simulation results of AoR, bulk density and  $p$  ratio for Sample 1 and 2.

## References

- [1] A. Van der Drift, H. Boerrigter, B. Coda, Entrained flow gasification of biomass., ECN - Energy Cent. Netherlands. (2004) 58. doi:10.1016/j.fuel.2011.10.063.
- [2] J.C. Vigié, N. Ullrich, P. Porot, L. Bournay, M. Hecquet, J. Rousseau, BioTfuel Project: Targeting the Development of Second-Generation Biodiesel and Biojet Fuels, *Oil Gas Sci. Technol.* 68 (2013) 935–946. doi:10.2516/ogst/2013162.
- [3] J. Dai, H. Cui, J.R. Grace, Biomass feeding for thermochemical reactors, *Prog. Energy Combust. Sci.* 38 (2012) 716–736. doi:10.1016/j.peccs.2012.04.002.
- [4] P.A. Cundall, O.D.L. Strack, A discrete numerical model for granular assemblies, *Géotechnique.* 29 (1979) 47–65. doi:10.1680/geot.1979.29.1.47.
- [5] Á. Ramírez-Gómez, E. Gallego, J.M. Fuentes, C. González-Montellano, F. Ayuga, Values for particle-scale properties of biomass briquettes made from agroforestry residues, *Particuology.* 12 (2014) 100–106. doi:10.1016/j.partic.2013.05.007.
- [6] M. Rackl, F. Top, C.P. Molhoek, D.L. Schott, Biomass and Bioenergy Feeding system for wood chips : A DEM study to improve equipment performance, *Biomass and Bioenergy.* 98 (2017) 43–52. doi:10.1016/j.biombioe.2017.01.003.
- [7] D. Ilic, K. Williams, R. Farnish, E. Webb, G. Liu, On the challenges facing the handling of solid biomass feedstocks, *Biofuels, Bioprod. Biorefining.* 12 (2018) 187–202. doi:10.1002/bbb.1851.
- [8] C. Hogue, Shape representation and contact detection for discrete element simulations of arbitrary geometries, 15 (1996) 374–390. doi:https://doi.org/10.1108/02644409810208525.
- [9] J.-P. Latham, A. Munjiza, The modelling of particle systems with real shapes., *Philos. Trans. A. Math. Phys. Eng. Sci.* 362 (2004) 1953–72. doi:10.1098/rsta.2004.1425.
- [10] Y. Guo, C. Wassgren, B. Hancock, W. Ketterhagen, J. Curtis, Computational study of granular shear flows of dry flexible fibres using the discrete element method, *J. Fluid Mech.* 775 (2015) 24–



52. doi:10.1017/jfm.2015.289.

- [11] Y. Guo, K. Buettner, V. Lane, C. Wassgren, W. Ketterhagen, B. Hancock, J. Curtis, Computational and Experimental Studies of Flexible Fiber Flows in a Normal-Stress-Fixed Shear Cell, *AICHE J.* (2018). doi:10.1002/aic.16397.
- [12] P. Pizette, N. Govender, D.N. Wilke, N. Abriak, New advances in large scale industrial DEM modeling towards energy efficient processes *Résumé : Abstract* :, (2017).
- [13] Y.T. Feng, D.R.J. Owen, Discrete element modelling of large scale particle systems—I: exact scaling laws, *Comput. Part. Mech.* 1 (2014) 159–168. doi:10.1007/s40571-014-0010-y.
- [14] Y.T. Feng, K. Han, D.R.J. Owen, J. Loughran, On upscaling of discrete element models: Similarity principles, *Eng. Comput.* (Swansea, Wales). 26 (2009) 599–609. doi:10.1108/02644400910975405.
- [15] T. Pöschel, C. Saluena, T. Schwager, Can we scale granular systems?, (2001).
- [16] J.E. Hilton, P.W. Cleary, Comparison of non-cohesive resolved and coarse grain DEM models for gas flow through particle beds, *Appl. Math. Model.* 38 (2014) 4197–4214. doi:10.1016/j.apm.2014.02.013.
- [17] D.S. Nasato, C. Goniva, S. Pirker, C. Kloss, Coarse graining for large-scale DEM simulations of particle flow - An investigation on contact and cohesion models, *Procedia Eng.* 102 (2015) 1484–1490. doi:10.1016/j.proeng.2015.01.282.
- [18] M. Sakai, S. Koshizuka, Large-scale discrete element modeling in pneumatic conveying, *Chem. Eng. Sci.* 64 (2009) 533–539. doi:10.1016/j.ces.2008.10.003.
- [19] T. Roessler, A. Katterfeld, Scaling of the angle of repose test and its influence on the calibration of DEM parameters using upscaled particles, *Powder Technol.* 330 (2018) 58–66. doi:10.1016/j.powtec.2018.01.044.
- [20] A.P. Grima, P.W. Wypych, Development and validation of calibration methods for discrete element modelling, *Granul. Matter.* 13 (2011) 127–132. doi:10.1007/s10035-010-0197-4.
- [21] M. Stahl, H. Konietzky, Discrete element simulation of ballast and gravel under special

- consideration of grain-shape, grain-size and relative density, *Granul. Matter.* 13 (2011) 417–428.  
doi:10.1007/s10035-010-0239-y.
- [22] M. Rackl, K.J. Hanley, A methodical calibration procedure for discrete element models, *Powder Technol.* 307 (2017) 73–83. doi:10.1016/j.powtec.2016.11.048.
- [23] S.C. Thakur, J.Y. Ooi, H. Ahmadian, Scaling of discrete element model parameters for cohesionless and cohesive solid, *Powder Technol.* 293 (2016) 130–137.  
doi:10.1016/j.powtec.2015.05.051.
- [24] H.Q. Do, A.M. Aragón, D.L. Schott, A calibration framework for discrete element model parameters using genetic algorithms, *Adv. Powder Technol.* (2018) 1–11.  
doi:10.1016/j.apt.2018.03.001.
- [25] H.Q. Do, A.M. Aragón, D.L. Schott, Automated discrete element method calibration using genetic and optimization algorithms, *EPJ Web Conf.* 140 (2017) 15011.  
doi:10.1051/epjconf/201714015011.
- [26] H.Q. Do, M. Mohajeri, D.L. Schott, CHoPS 2018 9 International Conference on Conveying and Handling of Particulate Solids CHoPS 2018 9 International Conference on Conveying and Handling of Particulate Solids, (2018) 1–6.
- [27] Y.H. Jung, H.J. Cho, J.S. Lee, E.W. Noh, O.K. Park, K.H. Kim, Evaluation of a transgenic poplar as a potential biomass crop for biofuel production, *Bioresour. Technol.* 129 (2013) 639–641.  
doi:10.1016/j.biortech.2012.12.074.
- [28] D. Dickmann, *Poplar culture in North America*, NRC Research Press, 2001.
- [29] Sympatec, QICPIC GmbH, (2018). <https://www.sympatec.com/en/particle-measurement/sensors/dynamic-image-analysis/qicpic/> (accessed July 11, 2018).
- [30] M. Combarros, H.J. Feise, H. Zetzener, A. Kwade, Segregation of particulate solids: Experiments and DEM simulations, *Particuology.* 12 (2014) 25–32. doi:10.1016/j.partic.2013.04.005.
- [31] P. Frankowski, M. Morgeneyer, Calibration and validation of DEM rolling and sliding friction

- coefficients in angle of repose and shear measurements, *AIP Conf. Proc.* 1542 (2013) 851–854.  
doi:10.1063/1.4812065.
- [32] S.M. Derakhshani, D.L. Schott, G. Lodewijks, Micro-macro properties of quartz sand: Experimental investigation and DEM simulation, *Powder Technol.* 269 (2015) 127–138.  
doi:10.1016/j.powtec.2014.08.072.
- [33] I.M.F. Wouters, D. Geldart, Characterising semi-cohesive powders using angle of repose, *Part. Part. Syst. Charact.* 13 (1996) 254–259. doi:10.1002/ppsc.19960130408.
- [34] D. Geldart, E.C. Abdullah, A. Hassanpour, L.C. Nwoke, I. Wouters, Characterization of powder flowability using measurement of angle of repose, *China Particuology.* 4 (2006) 104–107.  
doi:10.1016/S1672-2515(07)60247-4.
- [35] ImageJ, (n.d.). <https://imagej.nih.gov/ij/> (accessed July 30, 2018).
- [36] I. Darstellung, I.N. Kurzform, *Fm* 2 582, (1991).
- [37] M. Rackl, F.E. Grötsch, M. Rusch, J. Fottner, Qualitative and quantitative assessment of 3D-scanned bulk solid heap data, *Powder Technol.* 321 (2017) 105–118.  
doi:10.1016/j.powtec.2017.08.009.
- [38] M. Rackl, K.J. Hanley, A methodical calibration procedure for discrete element models, *Powder Technol.* 307 (2017) 73–83. doi:10.1016/j.powtec.2016.11.048.
- [39] J. Frańczek, A. Złobecki, J. Zemanek, Assessment of angle of repose of granular plant material using computer image analysis, (2007). doi:10.1016/j.jfoodeng.2006.11.028.
- [40] S.M. Derakhshani, *Modelling Dust Liberation in Bulk Material Handling Systems*, PhD thesis, Delft University of Technology, 2016. doi:10.4233/uuid:0d8c6401-fc4e-4b7b-babc-6eb9573d79b3.
- [41] ASTM International, D6773-02: Standard Test Method for Bulk Solids Using Schulze Ring Shear Tester 1, *Annu. B. ASTM Stand.* (2002) 1–26. doi:10.1520/D6682-08.
- [42] Jenike & Johanson, Ring Shear Tester, (2012). <http://jenike.com/bulkmaterialtesting/tester-supply/>.

- [43] D. Schulze, *Powders and Bulk Solids*, Springer Berlin Heidelberg, Berlin, Heidelberg, 2007.  
doi:10.1007/978-3-540-73768-1.
- [44] C. Kloss, C. Goniva, A. Hager, S. Amberger, S. Pirker, Models, algorithms and validation for opensource DEM and CFD-DEM, *Prog. Comput. Fluid Dyn. An Int. J.* 12 (2012) 140.  
doi:10.1504/PCFD.2012.047457.
- [45] C.G. DCS, gran model hertz model — LIGGGHTS v3.X documentation, Gran Hertz Model.  
(n.d.). [https://www.cfdem.com/media/DEM/docu/gran\\_model\\_hertz.html](https://www.cfdem.com/media/DEM/docu/gran_model_hertz.html) (accessed September 7, 2018).
- [46] Q.J. Zheng, H.P. Zhu, A.B. Yu, Finite element analysis of the rolling friction of a viscous particle on a rigid plane, *Powder Technol.* 207 (2011) 401–406. doi:10.1016/j.powtec.2010.11.026.
- [47] K. Iwashita, M. Oda, Rolling Resistance at Contacts in Simulation of Shear Band Development by DEM, *J. Eng. Mech.* 124 (1998) 285–292. doi:10.1061/(ASCE)0733-9399(1998)124:3(285).
- [48] J. Ai, J. Chen, J.M. Rotter, J.Y. Ooi, Assessment of rolling resistance models in discrete element simulations, *Powder Technol.* 206 (2011) 269–282. doi:10.1016/j.powtec.2010.09.030.
- [49] GmbH DCS Computing, gran cohesion sjkr model — LIGGGHTS v3.X documentation, (n.d.).  
[https://www.cfdem.com/media/DEM/docu/gran\\_cohesion\\_sjkr.html](https://www.cfdem.com/media/DEM/docu/gran_cohesion_sjkr.html) (accessed September 7, 2018).
- [50] L.B.J.F. Favier, MODELING NONSPHERICAL PARTICLES USING MULTISPHERE,  
(2001) 971–977.
- [51] M. Kodam, R. Bharadwaj, J. Curtis, B. Hancock, C. Wassgren, Cylindrical object contact detection for use in discrete element method simulations. Part I – Contact detection algorithms, (2010).  
doi:10.1016/j.ces.2010.08.006.
- [52] H. Kruggel-Emden, S. Rickelt, S. Wirtz, V. Scherer, A study on the validity of the multi-sphere Discrete Element Method, *Powder Technol.* 188 (2008) 153–165.  
doi:10.1016/j.powtec.2008.04.037.

- [53] D. Markauskas, Á. Ramírez-Gómez, R. Kačianauskas, E. Zdancevičius, Maize grain shape approaches for DEM modelling, *Comput. Electron. Agric.* 118 (2015) 247–258. doi:10.1016/j.compag.2015.09.004.
- [54] D. Markauskas, R. Kačianauskas, Investigation of rice grain flow by multi-sphere particle model with rolling resistance, *Granul. Matter.* 13 (2011) 143–148. doi:10.1007/s10035-010-0196-5.
- [55] F. Elskamp, H. Kruggel-Emden, M. Hennig, U. Teipel, A strategy to determine DEM parameters for spherical and non-spherical particles, *Granul. Matter.* 19 (2017) 1–13. doi:10.1007/s10035-017-0710-0.
- [56] Y. Li, Y. Xu, C. Thornton, A comparison of discrete element simulations and experiments for “sandpiles” composed of spherical particles, *Powder Technol.* 160 (2005) 219–228. doi:10.1016/j.powtec.2005.09.002.
- [57] O. Baran, A. DeGennaro, E. Ramé, A. Wilkinson, DEM simulation of a schulze ring shear tester, *AIP Conf. Proc.* 1145 (2009) 409–412. doi:10.1063/1.3179948.
- [58] R.S.T. Rst-xs, D. Schulze, Rst-control 95 xs, (2014).
- [59] Y.C. Zhou, B.H. Xu, A.B. Yu, P. Zulli, An experimental and numerical study of the angle of repose of coarse spheres, *Powder Technol.* 125 (2002) 45–54. doi:10.1016/S0032-5910(01)00520-4.
- [60] K. Deb, A. Pratap, S. Agarwal, T. Meyarivan, A fast and elitist multiobjective genetic algorithm: NSGA-II, *IEEE Trans. Evol. Comput.* 6 (2002) 182–197. doi:10.1109/4235.996017.
- [61] S. Mani, L.G. Tabil, S. Sokhansanj, Grinding performance and physical properties of wheat and barley straws, corn stover and switchgrass, *Biomass and Bioenergy.* 27 (2004) 339–352. doi:10.1016/j.biombioe.2004.03.007.
- [62] K.E. Ileleji, B. Zhou, The angle of repose of bulk corn stover particles, *Powder Technol.* 187 (2008) 110–118. doi:10.1016/j.powtec.2008.01.029.
- [63] S.L.C. Ferreira, A.O. Caires, T. da S. Borges, A.M.D.S. Lima, L.O.B. Silva, W.N.L. dos Santos,

- Robustness evaluation in analytical methods optimized using experimental designs, *Microchem. J.* 131 (2017) 163–169. doi:10.1016/j.microc.2016.12.004.
- [64] C.M. Wensrich, A. Katterfeld, Rolling friction as a technique for modelling particle shape in DEM, *Powder Technol.* 217 (2012) 409–417. doi:10.1016/j.powtec.2011.10.057.
- [65] © 2017 Minitab Inc., What is a main effects plot?, (n.d.). <http://support.minitab.com/en-us/minitab/17/topic-library/modeling-statistics/anova/basics/what-is-a-main-effects-plot/> (accessed September 17, 2018).
- [66] A.B. Zhou, Y. C.; Wright, B. D.; Yang, R. Y.; Xu, B. H; Yu, Rolling friction in the dynamic simulation of sandpile formation, *Phys. A Stat. Mech. Its Appl.* 269 (1999) 536–553. doi:10.1016/j.physa.2005.01.019.
- [67] T. Roessler, C. Richter, A. Katterfeld, F. Will, Development of a standard calibration procedure for the DEM parameters of cohesionless bulk materials – part I: Solving the problem of ambiguous parameter combinations, *Powder Technol.* (2018) #pagerange#. doi:10.1016/j.powtec.2018.11.034.
- [68] S.C. Thakur, J.P. Morrissey, J. Sun, J.F. Chen, J.Y. Ooi, Micromechanical analysis of cohesive granular materials using the discrete element method with an adhesive elasto-plastic contact model, *Granul. Matter.* 16 (2014) 383–400. doi:10.1007/s10035-014-0506-4.